Cratering Experiments on Granular Targets With a Variety of Particle Sizes: Implications for Craters on Rubble-Pile Asteroids

Yasui, Minami

Arakawa, Masahiko

Okawa, H.

Hasegawa, S.

(Citation)
Journal of Geophysical Research: Planets,127(8):e2021JE007172

(Issue Date)
2022-07-19

(Resource Type)
journal article

(Version)
Version of Record

JGR Planets

RESEARCH ARTICLE
10.1029/2021JE007172

Key Points:

- We performed cratering experiments on glass bead targets with a power-law bead size distribution at 50–4,400 m s^{-1}
- The size of craters formed in the mixed bead target was speculated to be changed with the size of the first contacted bead
- The armoring effect is less efficient for granular targets with a size distribution, compared with equal-sized granular targets

Supporting Information:

Supporting Information may be found in the online version of this article.

Correspondence to:

M. Yasui,
minami.yasui@pearl.kobe-u.ac.jp

Citation:

Yasui, M., Arakawa, M., Okawa, H., & Hasegawa, S. (2022). Cratering experiments on granular targets with a variety of particle sizes: Implications for craters on rubble-pile asteroids. *Journal of Geophysical Research: Planets*, *127*, e2021JE007172. https://doi.org/10.1029/2021JE007172

Received 4 JAN 2022
Accepted 9 JUL 2022

Author Contributions:

Conceptualization: M. Yasui, M. Arakawa
Data curation: H. Okawa
Formal analysis: M. Yasui
Funding acquisition: M. Yasui, M. Arakawa
Investigation: M. Yasui, M. Arakawa, H. Okawa, S. Hasegawa
Methodology: M. Yasui, M. Arakawa, H. Okawa, S. Hasegawa
Project Administration: M. Yasui, M. Arakawa, S. Hasegawa
Resources: M. Arakawa, S. Hasegawa
Supervision: M. Arakawa
Validation: M. Yasui, M. Arakawa
Visualization: M. Yasui
Writing – original draft: M. Yasui
Writing – review & editing: M. Yasui, M. Arakawa

Cratering Experiments on Granular Targets With a Variety of Particle Sizes: Implications for Craters on Rubble-Pile Asteroids

M. Yasui[1], M. Arakawa[1], H. Okawa[1], and S. Hasegawa[2]

[1]Graduate School of Science, Kobe University, Kobe, Japan, [2]Institute of Space and Astronautical Science, Japan Aerospace Exploration Agency, Sagamihara, Japan

Abstract We performed cratering experiments on targets composed of glass beads with a power-law size distribution that simulated the surface of rubble-pile asteroids, and we improved the previously studied reduction factor on the crater size scaling relationship including the armoring effect using the momentum transfer efficiency. Cratering experiments were conducted using light gas guns at Kobe University and ISAS/JAXA to control the impact velocity, v_i, from 50 to 4,400 m s^{-1}. Two kinds of mixed targets were prepared by mixing glass beads with diameters of 0.1, 1, 3, and 10 mm—one with the smallest diameter beads, and one without. The size ratio of the target bead to the projectile (diameter of 1–3 mm), ϕ, changed from 0.03 to 10. The crater size scaling relationships for the mixed targets were found to depend on the first contacted bead size. Notably, first contact with a 10 mm-sized bead reduced the crater radius by 35% in maximum. The reduction factor due to this armoring effect on the crater size scaling relationship is written as follows: $f(\phi) = \left[1 + \left(8.99 \times 10^{-3}\right) v_i^{0.63}\right]^{0.34} \phi^{-0.19}$; it decreased with the increase of the size ratio of the target bead to the projectile, while it increased with the increase of the impact velocity and approached unity. Our improved crater size scaling relationship that includes the reduction factor could be used to reconstruct the crater size frequency distribution on rubble-pile asteroids such as Ryugu, and it may lead to a revision of the crater chronology of asteroids.

Plain Language Summary A rubble-pile asteroid, 162173 Ryugu, was explored by Hayabusa2, and the crater size frequency distribution on the surface was examined. Ryugu's surface age can be estimated from this size distribution using the impact crater chronology, but the size of the asteroids forming the craters is necessary for this estimate. The crater size scaling law is used to estimate the impactor size, but this law was established using homogeneous grains such as granular sand, so it might not be applicable for rubble-pile asteroids covered with boulders of various sizes. Moreover, because it is well known that cratering efficiency is significantly reduced by an armoring effect when a smaller asteroid collides with a larger boulder, a scaling law that includes the armoring effect is required. In this study, we performed cratering experiments on the surface of simulated rubble-pile asteroids and examined the armoring effect on the crater size. Based on the results, we improved the previously studied armoring effect and introduced the momentum transfer efficiency, β, into the effect, instead of a restitution coefficient, which was assumed to be zero. Using this improved scaling relationship, a more accurate chronology can be established for the asteroid craters.

1. Introduction

Recent spacecraft explorations show that most rubble-pile asteroids are covered with many boulders of various sizes (Fujiwara et al., 2006; Lauretta et al., 2019; Watanabe et al., 2019). For example, the Hayabusa2 spacecraft observed that the asteroid (162173) Ryugu is covered with boulders for which the size frequency distribution follows the power law function with an exponent of −2.5 to −3 (Sugita et al., 2019). Moreover, boulders larger than 5 m size are distributed globally on Ryugu, and the power law index of the size distributions for these was estimated as -2.65 ± 0.05 (Michikami et al., 2019). From these observations, researchers initially expected that the size of the impact craters on Ryugu must be smaller than the estimate from the crater size π-scaling law in the gravity-dominated regime (Holsapple et al., 2002), which was established using granular materials with diameters much smaller than the impactor size (Arakawa et al., 2017). This is because the large boulders around the impact point would have been collapsed by the impact, resulting in a smaller crater size or no crater at all. This phenomenon is known as the armoring effect (Chapman et al., 2002; Hirata et al., 2009). However, the impactor

on Hayabusa2 impacted Ryugu and formed an artificial crater with a diameter of 14.5 m (SCI crater) (Arakawa et al., 2020). This crater diameter was almost the same as that estimated from the crater size scaling law of loose sand in the gravity regime (Housen & Holsapple, 2011), even if many boulders with a diameter larger than 13 cm, the diameter of the impactor, were distributed around the impact site of the SCI. On the other hand, the ejecta curtain of the SCI crater observed by the DCAM3 (Deployable CAMera 3) of Hayabusa2 was asymmetric and heterogeneous (Arakawa et al., 2020), unlike that observed for the granular materials that are typically used in laboratory experiments (e.g., Gault & Wedekind, 1978). From these observations, it is expected that the SCI crater size was not affected by large boulders but the heterogeneity of the SCI ejecta curtain could be affected by them.

Several researchers have carried out impact cratering experiments to examine the effect of the target particle size on the cratering process. Güttler et al. (2012) used glass beads as both projectile and target particle; the size ratio of the target bead to the projectile bead, ϕ, was 0.025–33.3 at an impact velocity of 200–300 m s^{-1}. They found that the cratering efficiency abruptly decreased when the size ratio was larger than 1, which they attributed to the armoring effect. Moreover, when the size ratio was larger than 3.3, beads at the impact point were disrupted or a crater formed on the beads. Tatsumi and Sugita (2018) used soda glass spheres, sintered glass beads, pumice grains, and basalt grains as a target; in their experiments, which were conducted with impact velocity of 70–6,000 m s^{-1}, the size ratio of the target grain to the projectile was ≥ 1. They established an improved crater size scaling relationship that includes the armoring effect. Barnouin et al. (2019) used glass beads as both projectile and target; in their experiments, which were conducted with impact velocity of 0.5–2.5 km s^{-1}, the size ratio was 1. They did not observe a reduction of the cratering efficiency, but they speculated that the first contacted point of the projectile on the target strongly influenced a crater shape, an ejection speed, and an ejection angle. Kadono et al. (2019) used mixed glass beads with diameters of 0.1 and 1 mm with various mass fractions as a target, and they reproduced the heterogeneous ejecta curtain due to 1 mm-diameter glass beads such as those observed on the SCI ejecta curtain.

Güttler et al. (2012) and Tatsumi and Sugita (2018) showed that the cratering efficiency was reduced by the armoring effect when the size ratio of the target grain to the projectile was larger than 1. However, they used almost uniformly sized target grains and thus did not consider the size distribution of grains in the target. Boulders on rubble-pile asteroids such as Ryugu, (101955) Bennu, and (25143) Itokawa have a power law-type size distribution. Thus, the effect of the boulder size distribution on the cratering efficiency should be studied. Barnouin et al. (2019) speculated that the initial contact between the projectile and the target grain at the impact was one of the key factor to control the cratering process. Therefore, the boulder size distribution and the size ratio of the first contacted boulder to the impactor are expected to be keys in controlling the crater size on rubble-pile asteroids.

The armoring effect could also affect the surface age of rubble-pile asteroids determined by a crater chronology (Tatsumi & Sugita, 2018). The surface age on a solid body is usually estimated by the crater chronology using the particular crater-size scaling relationship applicable to that solid body. On rubble-pile asteroids, the reduction rate of the cratering efficiency due to the armoring effect is necessary for determining the surface age, but it is not considered in the conventional crater size scaling law. Thus, a crater chronology with consideration for the armoring effect should be established. The surface age of Itokawa is estimated by using the scaling relationship including the armoring effect obtained by Tatsumi and Sugita (2018). They showed that the crater retention age on the surface of Itokawa was 3–33 Myrs. As in their study, when applying the crater chronology to the surface age on Ryugu and Bennu, it is necessary to determine a crater size scaling relationship that considers the effect of the boulder size distribution on the armoring effect.

In this study, we focused on the boulder size frequency distribution of rubble-pile asteroids such as Ryugu. Previous studies of Güttler et al. (2012), Tatsumi and Sugita (2018), and Barnouin et al. (2019) used targets composed of equal-sized grains. In order to apply the scaling relationship that introduces the armoring effect on asteroid surface with the boulder size frequency distribution, we conducted impact cratering experiments on glass bead targets having a power-law bead size distribution. Also, we focused on the first contact between the projectile and target glass bead, and improved the previously studied crater size scaling relationship, taking into account the armoring effect into a form that can be applied to asteroids with a boulder size distribution.

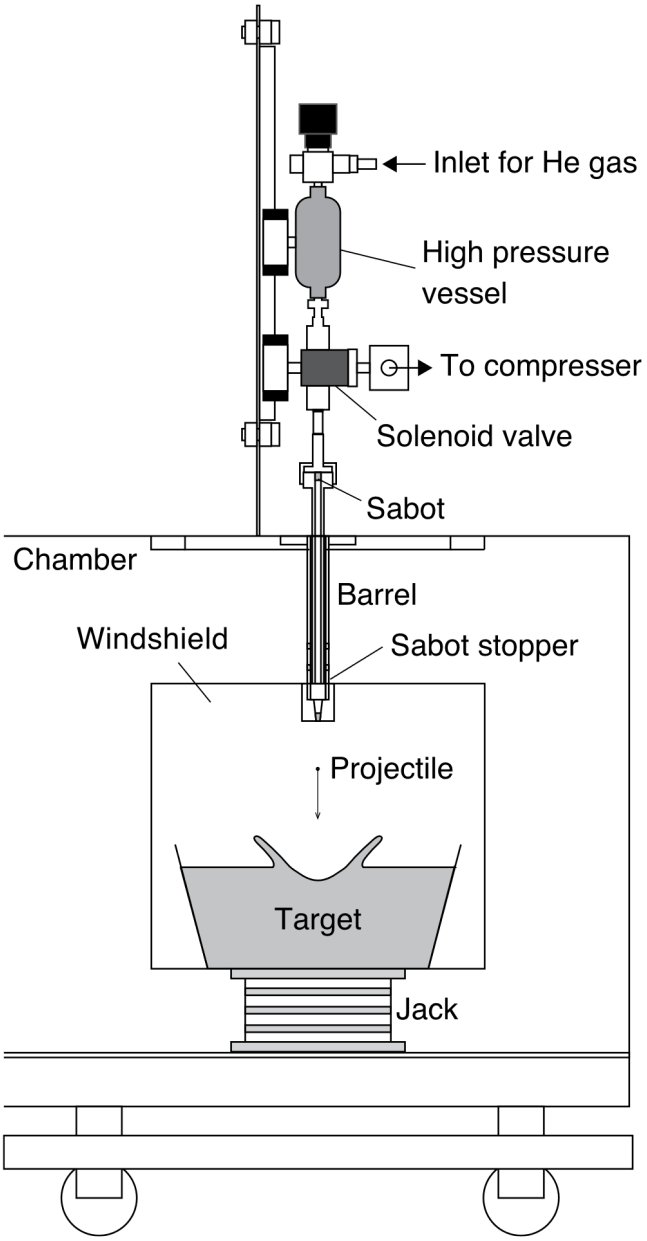

Figure 1. A schematic illustration of a one-stage small light gas gun at Kobe University.

2. Experimental Methods

We used glass beads with diameters of 0.1, 1, 3, and 10 mm as target particles. To simulate the regolith layer on rubble-pile asteroids such as Ryugu, we prepared two kinds of targets. One was composed of 0.1, 1, 3, and 10 mm-sized beads and was thus designated the "Mix F." The other was composed of 1, 3, and 10 mm-sized beads and was called the "Mix T" (Mix F without 0.1 mm-sized beads). For each target, glass beads of each size with the same mass fraction were mixed homogeneously. The power of the size frequency distributions for these mixed targets was −2.98, which is similar to the upper limit of the boulder distribution on Ryugu (Sugita et al., 2019) and slightly larger than the power of the size frequency distribution for the >5 m boulders globally distributed on Ryugu (Michikami et al., 2019). For comparison with the results of these mixed targets, we prepared a target composed of only 0.1 mm-sized glass beads. The calculated bulk density, ρ_b, and the measured angle of repose were 1.97 g cm^{-3} and 26.2 ± 1.1° for the Mix F, 1.68 g cm^{-3} and 28.6 ± 0.9° for the Mix T, and 1.42 g cm^{-3} and 25.1 ± 1.1° for the 0.1 mm target, respectively. The error of angle of repose is a standard deviation.

We conducted the impact experiments using multiple one-stage light gas guns at Kobe University and a two-stage light gas gun at ISAS/JAXA, depending on the impact velocity range and the projectile size. A projectile impacted the target surface normal to the gravity acceleration of Earth in all experiments. At Kobe University, a spherical projectile with a diameter of 2 mm was accelerated at an impact velocity of 51.4–145.3 m s^{-1} by using a small gas gun (Figure 1), while a 3 mm spherical projectile was accelerated at 84.2–208.3 m s^{-1} by using a mid-sized gas gun (Figure 3a in the paper of Tsujido et al., 2015). A projectile made of stainless steel (SUS, density of 7.8 g cm^{-3}) was used for the small gas gun. For the mid-sized gas gun, projectiles made of nylon (Ny, 1.2 g cm^{-3}), glass (Gl, 2.5 g cm^{-3}), alumina (Al_2O_3, 3.5 g cm^{-3}), titanium (Ti, 4.6 g cm^{-3}), zirconia (ZrO_2, 5.7 g cm^{-3}), SUS, and copper (Cu, 9.0 g cm^{-3}) were used, but the main projectiles used were Al_2O_3 and SUS projectiles. The glass beads were poured into containers with a diameter of 16 cm and depth of 6 cm for a small gas gun, and containers with 28 cm diameter and 10 cm depth for a mid-sized gas gun, respectively. The container was set in a vacuum chamber evacuated below 50 Pa for the small gas gun and below 10^3 Pa for the mid-sized gas gun; a chamber pressure below 10^3 Pa was confirmed not to affect the crater formation process (Suzuki et al., 2013). The detailed characteristics of these two gas guns are described in the paper of Tsujido et al. (2015).

In the case of the two-stage light gas gun at ISAS (Figure 1a in the paper of Matsue et al., 2020), spherical projectiles were accelerated at an impact velocity of 1.11–4.44 km s^{-1}. The projectiles were made of aluminum (Al, 2.7 g cm^{-3}), Ti, SUS, and Cu. The diameters of SUS projectiles were 1 and 2 mm, and the others were 1 mm. For the two-stage gas gun, glass beads were poured into a container of the same size of the mid-sized gas gun, which was set in a vacuum chamber evacuated below 5 Pa. The experimental setup is described in the paper of Matsue et al. (2020) in detail.

We measured the crater dimensions using three methods, depending on the target type. For the 0.1 mm target, we measured the rim-to-rim diameter, D_{rim}, by analyzing a photo taken from the top of the impact crater using a software, Image J. For the Mix T and F targets, we measured the D_{rim} by using a digital caliper just after the shot because the crater rim was unclear on the image. The rim-to-rim diameter for each shot was measured in four directions where they were crossed at ∼45°, so the D_{rim} is an average value and the standard deviation is

shown as an error. In addition, at ISAS, the crater profile was measured by using a 2D laser displacement meter (#LJ-V7300: Keyence; Osaka, Japan) with a resolution of 10 μm.

The impact was recorded using a high speed camera (Phantom v1612: Vision Research Inc.; Tokyo/MEMRE-CAM MX-5: nac Image Technology Inc.) with a framing rate of 2×10^3–10^5 frames per second to observe the ejecta curtain growth of the glass beads during the impact. For a detailed analysis of the ejecta growth, see Okawa et al. (2022).

3. Results

3.1. Crater Dimensions and Ejecta Curtain Growth

The experimental conditions and results are summarized in Table 1. Figures 2a and 2b show the crater profiles for the 0.1 mm target and the Mix F at impact velocities between 1.1 and 4.1 km s^{-1}, respectively. A photo of the impact crater on 0.1 mm target at 3.9 km s^{-1} in Figure 2a is shown in Figure 2d and a photo of Mix F at 4.1 km s^{-1} in Figure 2b is shown in Figure 2e. In the case of the 0.1 mm target, the impact crater is circular and it exhibited a distinct rim as shown on Figure 2d. These features were also observed on the other photos taken at the impact velocity of <200 m s^{-1}. The crater profiles on Figure 2a had a cone shape, and those normalized by the crater rim radius were matched with each other at all impact velocities: These impact craters show similarity. In the case of the Mix F, the crater shape was irregular and complex, not circular, and the rim was unclear as shown on Figure 2a. On the crater profiles (Figure 2b), the craters appeared bumpy and the elevation of the crater surface relative to pre-shot surface varied within 10 mm due to the variously sized glass beads and because the laser of the displacement meter passed through 3 and 10 mm-sized beads, but the overview of the profiles showed a roughly cone shape. The crater profiles normalized by the crater rim radius were almost matched with each other. These features are also clear on the profiles measured from two different directions in each shot (Figure S1 in Supporting Information S1). By analyzing the crater profiles at the impact velocity of >1.1 km s^{-1} for the 0.1 mm and Mix F, the ratio of the crater rim radius to the apparent crater radius on the pre-shot target surface, $R_{\rm rim}/R$, could be determined as shown in Figure 2c. The $R_{\rm rim}$ is defined as $D_{\rm rim} = 2R_{\rm rim}$, and the $R_{\rm rim}/R$ was 1.17 ± 0.05 for the 0.1 mm target and 1.22 ± 0.05 for the Mix F, respectively. This $R_{\rm rim}/R$ ratio was necessary to construct a crater size scaling relationship based on R.

The ejecta curtains at the crater formation time τ are shown on Figures 2f and 2g. These high-speed movies are included in Movies S1 and S2. The τ is calculated by $\sqrt{R/g}$, where the g is the gravitational acceleration. The ejecta curtain made of granular materials is known to have an inverted cone shape (e.g., Gault & Wedekind, 1978), and our 0.1 mm target had a similar shape (Figure 2f and Movie S1). On the other hand, the Mix F also had a similar shape, but it showed a different structure on the ejecta curtain surface (Figure 2g). The beads with diameters of 1 and 3 mm ejected dispersedly that each bead could be identified, but the curtain appeared heterogeneous and asymmetric, compared with that for the 0.1 mm target. In addition, the structure formed by the 0.1 mm-sized beads appeared wavy and exhibited strong contrast: These features might have been due to disturbance from the larger beads. This structure is similar to that of the targets mixed with 0.1 and 1 mm-sized glass beads (Kadono et al., 2019). We found on the movie (Movie S2 in Supporting Information S3) that a few 10 mm-sized beads were ejected from the crater, and some of them crawled slowly on the target surface, although most of them remained in their initial positions.

3.2. Crater Radius

Figure 3a shows the relationship between the crater rim diameter, $D_{\rm rim}$, and the kinetic energy of the projectile, $E_{\rm k}$, for all data. The $D_{\rm rim}$ increased with the increase of the $E_{\rm k}$ for each target. Moreover, the $D_{\rm rim}$ of the 0.1 mm target was larger than those of the Mix T and F. The $D_{\rm rim}$ values of the Mix T and F were almost identical, irrespective of the presence or absence of 0.1 mm-sized beads, although they were a little scattered compared with that of the 0.1 mm target. On some shots for the Mix T and F, the projectile was speculated to directly impact on a 10 mm-sized glass bead on the target surface because we recovered a 10 mm-sized bead on which a few cracks were formed at <210 m s^{-1} or some fragments with a partially rounded surface at >1 km s^{-1}. We thus call this case as a "C-10" target when the size of a first contact bead was 10 mm. The $D_{\rm rim}$ values of the "C-10" targets were somewhat scattered, but they were smaller than those of the Mix T and F. Furthermore, the "C-10" targets accounted for 62% of the total data in the Mix T, which was larger than the 15% of "C-10" data in the Mix F. This is because both the volume fraction of 10 mm-sized glass beads to all beads on the target surface and the

Journal of Geophysical Research: Planets

10.1029/2021JE007172

Table 1
Experimental Conditions and Results

Target velocity range	Run number	Projectile: Material	Projectile: Mass (m_p), mg	Projectile: Diameter ($d_p = r_p/2$), mm	Impact velocity (v_i), m s^{-1}	Kinetic energy (E_k), JJ	Crater rim diameter (D_{rim}), mm: Average	Crater rim diameter (D_{rim}), mm: Error	R_{rim}/R^{**}	π_2	π_4	π_R: Average	π_R: Error	$\pi_R/\pi_4{}^c$	"C-10"
0.1 mm target Low velocity	180427-1	SUS	32.77	1.996	124.8	0.255	64.50	0.672	–	6.28E-07	0.18	9.23	0.096	10.3	
	180427-2	SUS	32.77	1.996	97.4	0.155	56.36	1.49	–	1.03E-06	0.18	8.06	0.213	9.03	
	180427-3	SUS	32.77	1.996	110.0	0.198	63.12	0.905	–	8.08E-07	0.18	9.03	0.129	10.1	
	180427-4	SUS	32.77	1.996	91.0	0.136	54.95	2.94	–	1.18E-06	0.18	7.86	0.421	8.80	
	180628-1	SUS	32.78	2.003	104.3	0.178	60.32	0.735	–	9.03E-07	0.18	8.63	0.105	9.66	
	180628-2	SUS	32.78	2.003	97.3	0.155	59.02	0.339	–	1.04E-06	0.18	8.44	0.049	9.45	
	180628-3	SUS	32.78	2.003	127.9	0.268	67.51	0.0566	–	6.00E-07	0.18	9.66	0.008	10.8	
	180702-1	SUS	32.75	1.998	87.4	0.125	55.71	1.05	–	1.28E-06	0.18	7.97	0.151	8.92	
	180702-2	SUS	32.75	1.998	102.5	0.172	60.90	0.354	–	9.32E-07	0.18	8.71	0.051	9.76	
	180702-3	SUS	32.75	1.998	102.6	0.172	58.61	0.170	–	9.30E-07	0.18	8.39	0.024	9.39	
	180702-4	SUS	32.75	1.998	104.6	0.179	61.78	0.453	–	8.95E-07	0.18	8.84	0.065	9.90	
	180702-5	SUS	32.75	1.998	107.5	0.189	62.47	0.431	–	8.47E-07	0.18	8.94	0.062	10.0	
	180702-6	SUS	32.75	1.998	122.5	0.246	66.87	0.205	–	6.52E-07	0.18	9.57	0.029	10.7	
	180702-7	SUS	32.75	1.998	104.1	0.177	60.93	0.990	–	9.04E-07	0.18	8.72	0.142	9.76	
	180702-8	SUS	32.75	1.998	123.7	0.251	65.91	0.007	–	6.39E-07	0.18	9.43	0.001	10.6	
	180704-1	SUS	32.75	1.998	85.9	0.121	55.74	0.255	–	1.33E-06	0.18	7.98	0.036	8.93	
	180704-2	SUS	32.75	1.998	87.8	0.126	57.83	0.983	–	1.27E-06	0.18	8.27	0.141	9.26	
	180704-3	SUS	32.75	1.998	70.9	0.0822	53.00	0.346	–	1.95E-06	0.18	7.58	0.050	8.49	
	180704-4	SUS	32.75	1.998	77.8	0.0992	54.59	0.552	–	1.62E-06	0.18	7.81	0.079	8.75	
	180704-5	SUS	32.75	1.998	68.2	0.0762	52.34	0.757	–	2.11E-06	0.18	7.49	0.108	8.38	
	180704-6	SUS	32.75	1.998	118.6	0.230	66.90	1.27	–	6.96E-07	0.18	9.57	0.182	10.7	
	180704-7	SUS	32.75	1.998	118.0	0.228	65.81	1.27	–	7.03E-07	0.18	9.42	0.182	10.5	
	180705-1	SUS	32.75	1.998	145.3	0.346	68.51	0.445	–	4.64E-07	0.18	9.80	0.064	11.0	
	180705-2	SUS	32.75	1.998	63.5	0.0660	49.32	1.24	–	2.43E-06	0.18	7.06	0.177	7.90	
	180705-3	SUS	32.75	1.998	73.4	0.0882	53.36	1.61	–	1.82E-06	0.18	7.64	0.231	8.55	
	180705-4	SUS	32.75	1.998	62.4	0.0638	50.74	1.39	–	2.51E-06	0.18	7.26	0.199	8.13	
	180705-5	SUS	32.75	1.998	55.0	0.0496	45.78	0.566	–	3.23E-06	0.18	6.55	0.081	7.33	
	181119-1	SUS	32.76	2.003	82.1	0.110	55.12	0.413	–	1.45E-06	0.18	7.89	0.059	8.83	
	181119-2	SUS	32.76	2.003	104.5	0.179	62.69	1.25	–	8.98E-07	0.18	8.97	0.179	10.0	
	181119-3	SUS	32.76	2.003	100.0	0.164	61.35	0.095	–	9.81E-07	0.18	8.78	0.014	9.82	

Journal of Geophysical Research: Planets

10.1029/2021JE007172

Table 1
Continued

Target velocity range	Run number	Projectile			Impact velocity (v_i), m s^{-1}	Kinetic energy (E_k), JJ	Crater rim diameter (D_{rim}), mm		R_{rim}/R^{**}	π_2	π_4	π_R		$\pi_R/\pi_4{}^c$	"C-10"
		Material	Mass (m_p), mg	Diameter ($d_p = r_p/2$), mm			Average	Error				Average	Error		
	181119-4	SUS	32.76	2.003	141.3	0.327	71.50	0.043	–	4.92E-07	0.18	10.23	0.006	11.4	
	181119-5	SUS	32.76	2.003	51.4	0.0432	46.37	0.362	–	3.72E-06	0.18	6.63	0.052	7.43	
0.1 mm target High velocity	190626-2	Al	1.49	1.003	1113	0.923	59.76	1.12	1.21	3.97E-09	0.50	23.1	0.431	24.1	
	190626-3	Al	1.44	1.002	2554	4.70	71.85	1.42	1.20	7.53E-10	0.52	28.4	0.561	29.7	
	190626-4	Al	1.34	1.006	4057	11.0	83.38	0.924	1.27	2.99E-10	0.57	31.9	0.353	33.1	
	190626-5	Al	1.42	1.000	2657	5.01	73.19	1.23	1.21	6.94E-10	0.52	28.8	0.483	30.0	
	190626-6	Al	1.40	0.999	1152	0.929	58.45	1.12	1.16	3.69E-09	0.53	24.2	0.465	25.2	
	200930-4	SUS	4.19	0.998	1185	2.94	79.92	1.44	1.20	3.48E-09	0.18	22.2	0.399	24.9	
	200930-5	SUS	4.21	0.998	2129	9.54	93.54	1.01	1.16	1.08E-09	0.18	26.8	0.291	30.1	
	201001-1	SUS	4.02	0.997	4417	39.2	112.99	1.11	1.14	2.50E-10	0.18	33.3	0.327	37.3	
	201001-2	SUS	33.50	2.00	4132	286	192.29	3.20	1.06	5.74E-10	0.18	30.0	0.500	33.7	
	201002-6	SUS	33.50	2.00	4098	281	198.92	1.36	–	5.84E-10	0.18	28.2	0.192	31.6	
	210317-8	SUS	3.87	1.00	4419	37.8	110.40	1.59	–	2.51E-10	0.19	32.1	0.462	35.8	
	210318-1	SUS	33.30	2.00	1925	61.7	164.66	0.809	1.15	2.64E-09	0.18	23.8	0.117	26.7	
	210318-3	SUS	3.81	1.00	4355	36.1	114.70	0.637	1.18	2.58E-10	0.20	33.3	0.185	37.1	
	210318-4	SUS	33.40	2.00	1943	63.0	166.88	1.52	1.12	2.60E-09	0.18	24.7	0.225	27.7	
Mix T Low velocity	180924-1	SUS	112.0	3.00	159.7	1.43	83.29	1.04	–	5.76E-07	0.21	8.42	0.105	8.73	
	180924-2	SUS	112.0	3.00	180.5	1.82	69.90	1.87	–	4.51E-07	0.21	7.07	0.189	7.33	*
	180924-3	SUS	112.0	3.00	152.0	1.29	56.34	1.98	–	6.36E-07	0.21	5.70	0.201	5.91	*
	180924-4	Al_2O_3	46.0	3.00	145.8	0.489	50.90	0.969	–	6.92E-07	0.52	6.93	0.132	7.03	*
	180924-5	Al_2O_3	50.0	3.00	99.6	0.248	43.19	0.683	–	1.48E-06	0.48	5.72	0.090	5.82	*
	180924-6	SUS	113.0	3.00	117.6	0.782	65.44	7.24	–	1.06E-06	0.21	6.60	0.730	6.84	*
	181116-1	SUS	32.68	2.00	81.4	0.108	48.97	2.62	–	1.48E-06	0.22	7.47	0.400	7.74	
	181116-2	SUS	32.68	2.00	104.9	0.180	53.27	1.68	–	8.91E-07	0.22	8.12	0.256	8.42	
	181116-3	SUS	32.68	2.00	117.0	0.224	53.83	1.73	–	7.16E-07	0.22	8.21	0.264	8.51	
	181116-4	SUS	32.68	2.00	131.5	0.282	58.07	1.19	–	5.67E-07	0.22	8.86	0.182	9.18	
Mix T High velocity	201001-4	Al	1.59	0.990	4344	15.0	73.66	1.82	–	2.57E-10	0.54	29.0	0.718	29.0	*

Journal of Geophysical Research: Planets

10.1029/2021JE007172

Table 1
Continued

Target velocity range	Run number	Projectile			Impact velocity (v_i), m s^{-1}	Kinetic energy (E_k), JJ	Crater rim diameter (D_{rim}), mm		R_{rim}/R^{**}	π_2	π_4	π_R		$\pi_R/\pi_4{}^c$	"C-10"
		Material	Mass (m_p), mg	Diameter ($d_p = r_p/2$), mm			Average	Error				Average	Error		
	201001-5	SUS	4.12	0.995	4344	38.9	95.06	3.10	–	2.58E-10	0.21	27.3	0.887	27.3	*
	201001-6	SUS	4.00	0.995	1181	2.79	54.38	3.71	–	3.50E-09	0.22	15.7	1.07	15.7	*
Mix F Low velocity	180711-1	SUS	32.75	1.998	126.6	0.263	52.09	0.120	–	6.11E-07	0.25	7.94	0.018	8.20	
	180711-2	SUS	32.95	2.005	140.9	0.327	62.32	2.22	–	4.95E-07	0.25	9.48	0.337	9.79	
	180711-3	SUS	32.95	2.005	82.6	0.112	41.51	1.47	–	1.44E-06	0.25	6.31	0.223	6.52	
	180711-4	SUS	32.95	2.005	60.4	0.060	39.62	2.58	–	2.70E-06	0.25	6.03	0.393	6.22	
	180712-1	SUS	32.66	2.001	128.6	0.270	56.87	0.861	–	5.93E-07	0.25	8.67	0.131	8.96	
	180712-2	SUS	32.71	2.004	113.2	0.209	50.97	2.27	–	7.67E-07	0.25	7.77	0.346	8.02	
	180712-3	SUS	32.71	2.004	79.5	0.103	41.19	1.45	–	1.55E-06	0.25	6.28	0.221	6.48	
	180712-4	SUS	32.71	2.004	65.4	0.0699	40.87	1.72	–	2.30E-06	0.25	6.23	0.262	6.43	
	180713-1	SUS	32.71	2.004	112.2	0.206	53.36	2.95	–	7.81E-07	0.25	8.14	0.450	8.40	
	180713-2	SUS	32.78	1.999	81.1	0.108	40.38	3.44	–	1.49E-06	0.25	6.15	0.524	6.35	*
	180713-3	SUS	32.78	1.999	81.3	0.108	33.74	1.79	–	1.48E-06	0.25	5.14	0.273	5.31	*
	180718-1	SUS	32.78	1.999	117.9	0.228	52.91	3.03	–	7.04E-07	0.25	8.06	0.462	8.32	
	180718-2	SUS	32.78	1.999	63.7	0.067	32.47	2.17	–	2.41E-06	0.25	4.95	0.330	5.11	*
	180718-3	SUS	32.78	1.999	143.3	0.337	57.85	2.77	–	4.77E-07	0.25	8.81	0.421	9.10	
	180718-4	SUS	32.78	1.999	125.8	0.259	48.62	0.770	–	6.19E-07	0.25	7.41	0.117	7.65	
	180718-5	SUS	32.78	1.999	82.0	0.110	31.15	0.680	–	1.46E-06	0.25	4.75	0.104	4.90	*
	180718-6	SUS	32.64	2.002	53.2	0.0463	38.48	1.25	–	3.46E-06	0.25	5.87	0.190	6.06	
	180719-1	SUS	32.64	2.002	98.5	0.158	47.33	1.52	–	1.01E-06	0.25	7.22	0.232	7.45	
	180719-2	SUS	32.64	2.002	99.8	0.162	45.32	1.62	–	9.86E-07	0.25	6.92	0.247	7.14	
	180719-3	SUS	32.64	2.002	98.0	0.157	45.68	1.28	–	1.02E-06	0.25	6.97	0.195	7.20	
	191112-1	Al_2O_3	55.0	3.03	105.9	0.309	58.92	0.970	–	1.32E-06	0.52	7.55	0.124	7.67	
	191113-1	Al_2O_3	58.0	3.06	200.8	1.17	69.80	1.61	–	3.72E-07	0.51	8.79	0.203	8.93	
	191113-2	Al_2O_3	58.0	3.06	180.5	0.945	66.24	2.63	–	4.60E-07	0.51	8.34	0.331	8.48	
	191113-3	Al_2O_3	58.0	3.06	180.5	0.945	68.41	1.35	–	4.60E-07	0.51	8.62	0.170	8.75	
	191113-4	Al_2O_3	58.0	3.06	208.3	1.26	73.94	1.56	–	3.45E-07	0.51	9.31	0.196	9.46	
	191113-5	Al_2O_3	58.0	3.06	179.2	0.931	62.45	2.65	–	4.67E-07	0.51	7.87	0.333	7.99	*
	191113-6	Al_2O_3	47.0	2.92	84.2	0.167	51.99	2.08	–	2.02E-06	0.55	7.02	0.282	7.12	

Journal of Geophysical Research: Planets

10.1029/2021JE007172

Table 1
Continued

Target velocity range	Run number	Projectile			Impact velocity (v_i), m s^{-1}	Kinetic energy (E_k), JJ	Crater rim diameter (D_{rim}), mm		R_{rim}/R**	π_2	π_4	π_R		$\pi_R/\pi_4{}^c$	"C-10"
		Material	Mass (m_p), mg	Diameter ($d_p = r_p/2$), mm			Average	Error				Average	Error		
	191114-1	Ny	19.0	3.16	185.2	0.326	50.10	2.99	–	4.52E-07	1.71	9.16	0.545	9.04	
	191114-2	Gl	27.0	2.67	174.2	0.410	55.01	2.84	–	4.31E-07	0.73	8.94	0.462	9.01	
	191114-3	Ti	63.0	2.99	164.5	0.852	62.24	2.21	–	5.42E-07	0.44	7.63	0.270	7.77	
	191114-4	ZrO_2	81.0	2.94	134.8	0.736	66.80	4.07	–	7.93E-07	0.32	7.53	0.459	7.73	
	191114-5	SUS	112.0	2.99	168.9	1.60	85.53	3.56	–	5.13E-07	0.25	8.65	0.361	8.94	
	191114-6	Cu	129.0	3.01	177.9	2.04	89.25	5.25	–	4.66E-07	0.22	8.61	0.506	8.92	
	191114-7	ZrO_2	81.0	2.94	172.4	1.20	77.86	3.78	–	4.85E-07	0.32	8.77	0.426	9.01	
	191114-8	Ti	64.0	2.98	129.2	0.534	71.25	2.21	–	8.75E-07	0.43	8.68	0.269	8.86	
Mix F High velocity	190201-1	Al	1.51	0.986	1215	1.11	48.91	1.56	1.24	3.27E-09	0.66	19.4	0.617	19.4	
	190201-2	Al	1.58	0.987	4438	15.6	81.62	2.05	1.28	2.46E-10	0.63	30.9	0.774	30.9	*
	190201-4	Al	1.50	0.995	2818	5.96	69.44	1.22	–	6.14E-10	0.68	27.9	0.491	27.9	
	190930-1	Al	1.46	1.000	1178	1.01	50.91	1.11	–	3.53E-09	0.71	20.6	0.450	20.6	
	191001-1	Al	1.40	1.000	2269	3.60	66.76	0.599	1.21	9.52E-10	0.74	27.8	0.249	27.8	
	191001-2	Al	1.33	0.990	3909	10.2	74.81	1.19	–	3.17E-10	0.75	31.3	0.496	31.3	
	191001-3	SUS	4.06	0.991	2192	9.75	79.93	2.63	1.14	1.01E-09	0.25	24.7	0.810	24.7	
	191001-4	SUS	4.14	0.991	2311	11.1	74.85	3.14	–	9.09E-10	0.24	21.4	0.899	21.4	*
	191001-5	SUS	4.07	0.992	4134	34.8	91.50	4.41	–	2.84E-10	0.25	26.3	1.27	26.3	
	191001-6	SUS	3.97	0.998	4263	36.1	109.86	2.71	–	2.69E-10	0.26	31.9	0.788	31.9	
	191001-7	SUS	4.35	1.000	1181	3.03	65.83	2.83	–	3.51E-09	0.24	18.5	0.797	18.5	
	191002-1	Al	1.43	0.995	1189	1.01	40.93	0.552	–	3.45E-09	0.71	16.7	0.225	16.7	*
	191106-5	Al	1.44	0.996	1201	1.04	47.36	2.66	1.17	3.38E-09	0.71	20.2	1.14	20.2	
	191106-6	SUS	3.81	0.970	1232	2.89	70.57	1.22	1.29	3.13E-09	0.25	19.7	0.339	19.7	
	191107-1	SUS	4.02	0.996	4303	37.2	103.56	3.56	1.23	2.64E-10	0.25	29.7	1.02	29.7	
	191107-2	Ti	2.38	0.999	4279	21.8	91.21	3.32	1.27	2.67E-10	0.43	30.4	1.10	30.4	
	191107-3	Cu	4.78	1.006	4299	44.2	113.65	4.04	1.19	2.67E-10	0.22	31.8	1.13	31.8	

Note. An asterisk * on the line of "C-10" shows the experimental result when the projectile collided with a 10 mm-sized glass bead on the target surface. The details are explained in Section 3.2. The R_{rim}/R shown by a double asterisk ** is measured using a crater profile. On a shot shown as "–", the crater profile was not measured or the crater rim and the pre-impact surface were not clear due to large bumps on the crater profile.

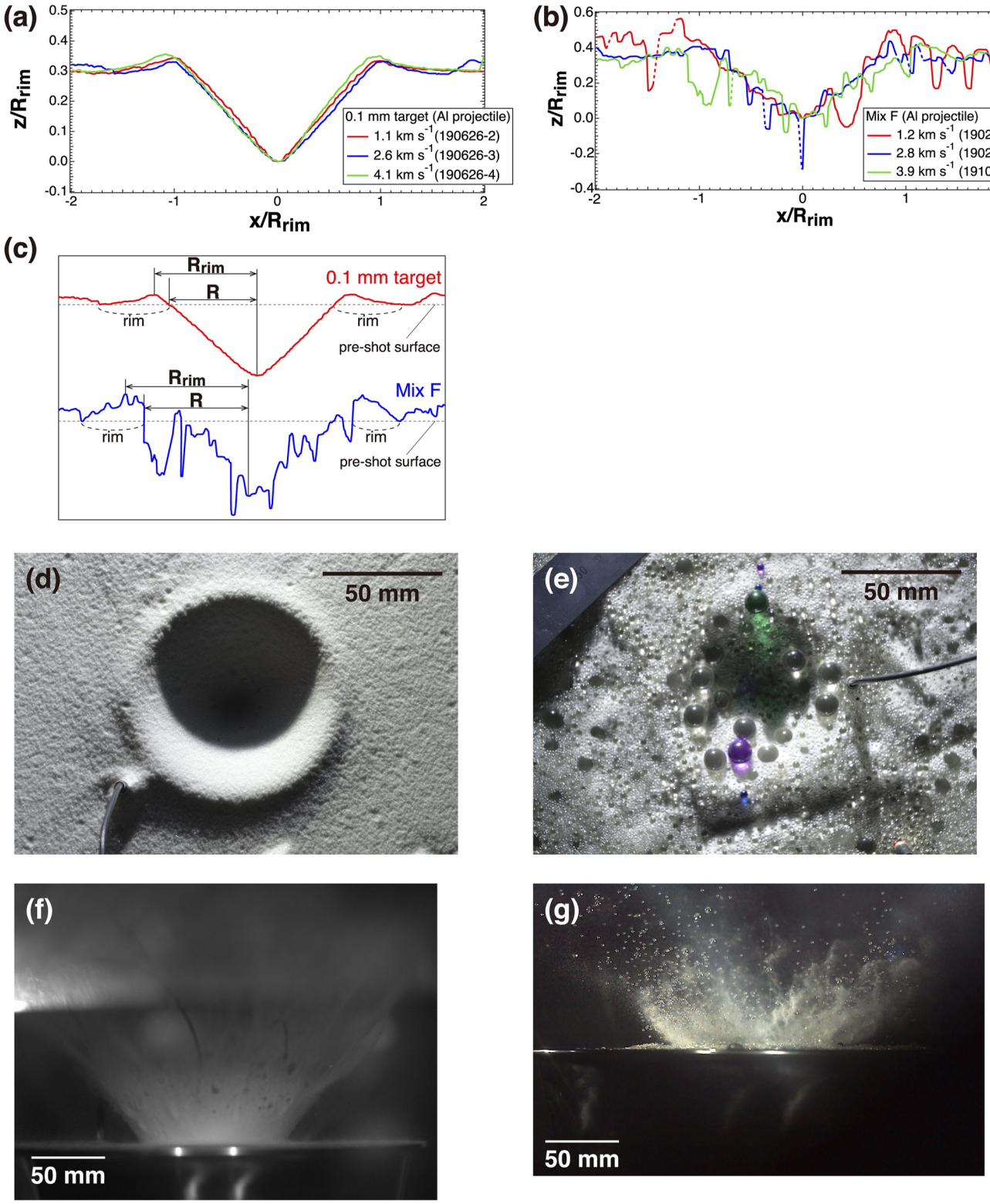

Figure 2. (a, b) Crater profiles for (a) 0.1 mm targets and (b) Mix F, at the impact velocities of 1.1–1.2 km s^{-1}, 2.6–2.8 km s^{-1}, and 3.9–4.1 km s^{-1}. The units shown on both axes are normalized by the crater rim radius, R_{rim}. The number in the parentheses on the legend is the run number. The dashed lines in panel (b) are the linearly interpolated lines between the acquired data points. Some data points were withheld due to measurement error. (c) Definitions of the crater rim radius, R_{rim}, and crater radius, R, for the 0.1 mm target and Mix F. The crater profiles are the same as that of panel (a) at 4.1 km s^{-1} and panel (b) at 3.9 km s^{-1}. (d, e) Photos of the impact crater taken from the top of (d) the 0.1 mm target (run number: 190626-4) and (e) the Mix F (run number: 191001-2). (f, g) Ejecta curtain observed at the crater formation time for (f) the 0.1 mm target (run number: 190626-4) and (g) the Mix F (run number: 191001-2).

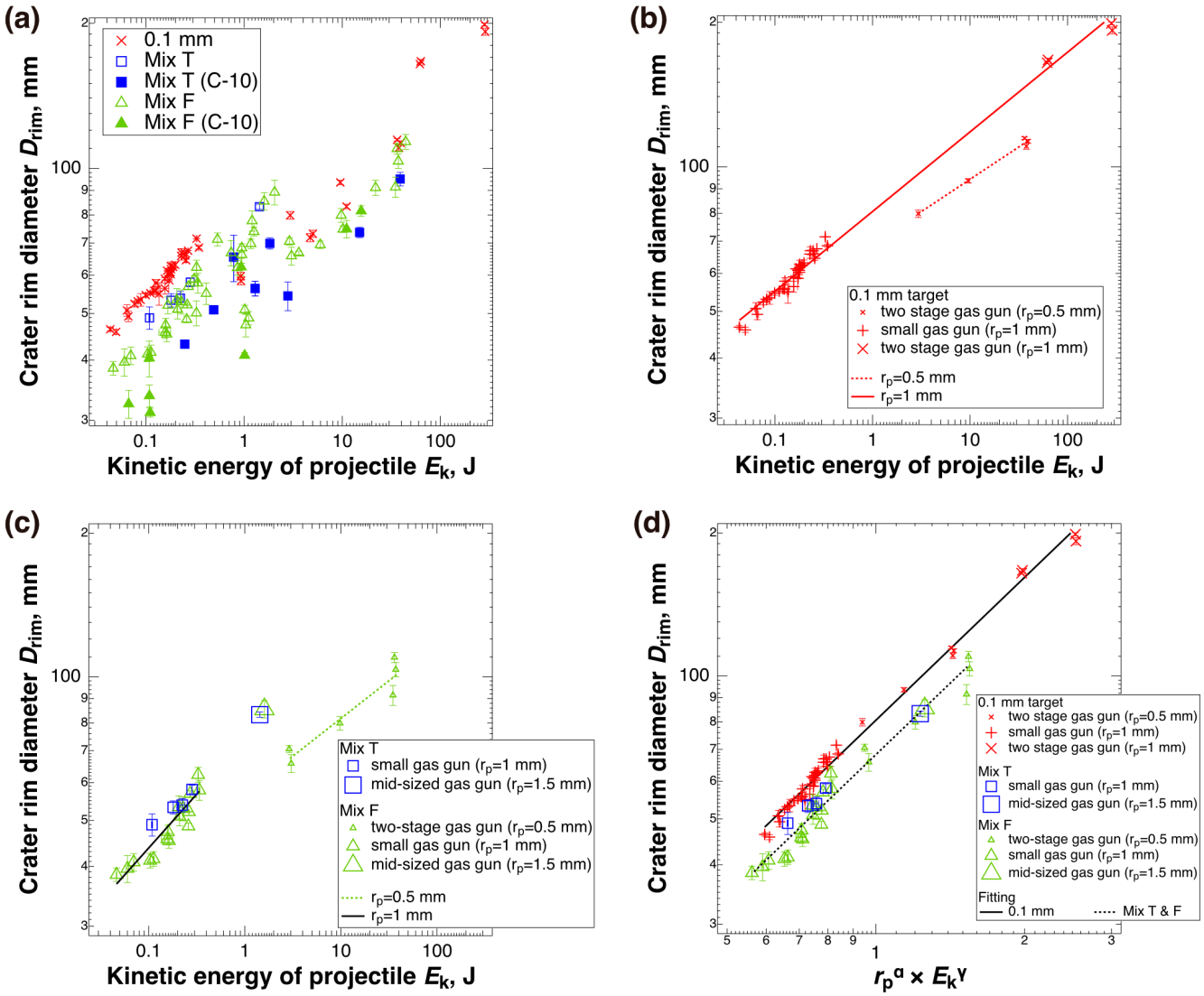

Figure 3. Relationship between the crater rim diameter, D_{rim}, and the kinetic energy of the projectile, E_k, for (a) all data, (b) 0.1 mm targets, and (c) Mix T and F. Panels (b) and (c) show the data for SUS projectiles with different radii at different impact velocity ranges. The solid lines are fitting lines generated using the power-law equations. (d) Relationship between the crater rim diameter, D_{rim}, and $r_p^{\alpha} E_k^{\gamma}$ for 0.1 mm targets and Mix T and F.

porosity of the Mix T were larger than those of the Mix F. Thus, the probability of impact with a 10 mm-sized bead on the Mix T surface might have been higher.

As shown in Figure 3a, the D_{rim} increased continuously with the increase of the E_k for small E_k, but it dropped abruptly for E_k =1–2 J for each target. In order to examine this gap in detail, the relationship between the D_{rim} and the E_k with SUS projectiles is shown for the 0.1 mm target on Figure 3b, and for Mix T and F on Figure 3c. In these figures, the D_{rim} depends on not only the E_k but also the projectile radius, r_p. In Figure 3b, it can be seen that the D_{rim} for 2 mm-sized SUS projectiles had the same relationship, even if the impact velocity differed by one order of magnitude. Furthermore, the D_{rim} for 1 mm-sized SUS projectiles was systematically smaller than that for 2 mm-sized SUS projectiles. A similar dependence on the r_p was also confirmed for the Mix T and F in Figure 3c. Moreover, the D_{rim} for the Mix T was almost consistent with that for the Mix F with same r_p. However, the range of the size ratio of the target bead to the projectile, $\phi = r_t/r_p$, which r_t is the radius of the target bead, was quite different between the 0.1 mm target and Mix T and F. That is, the range was 0.05–0.1 for the 0.1 mm target but 0.03–10 for the Mix T and F. So, the dependence of D_{rim} on the r_p could be affected by this size ratio range. In order to study this dependence, a multivariate analysis was conducted for the variables D_{rim}, r_p, and E_k.

The results showed that D_{rim} could be well scaled with $r_{\mathrm{p}}^{\alpha}E_{\mathrm{k}}^{\gamma}$, and the α was 0.35 ± 0.06 for both targets as shown in Figure 3d. Thus, the ϕ range did not affect the D_{rim} against the r_{p}. The γ was 0.17 ± 0.003 for the 0.1 mm target and 0.18 ± 0.01 for the Mix T and F, and an offset was found between them. These differences might have been caused by the difference in the physical properties of the target, such as the density and angle of repose.

3.3. Crater Size Scaling Relationship

We organized our experimental results on the crater radius in order to improve the π-scaling law proposed by Housen et al. (1983) and Housen and Holsapple (2011); this conventional scaling law is often used to relate the laboratory-scaled results to the planetary-scaled impact phenomena. The crater size scaling law that we used is in the gravity-dominated regime, not the strength-dominated regime, and it is written as follows:

$$R\left(\frac{\rho_{\mathrm{b}}}{m_{\mathrm{p}}}\right)^{\frac{1}{3}} = H_1\left(\frac{gr_{\mathrm{p}}}{v_{\mathrm{i}}^2}\right)^{b}\left(\frac{\rho_{\mathrm{b}}}{\delta}\right)^{c}, \quad (1)$$

where m_{p} is the projectile mass, r_{p} is the projectile radius, δ is the density of the projectile, ρ_{b} is the bulk density of the target, and v_{i} is the impact velocity. H_1, b, and c are constants; b and c are rewritten by using the coupling parameter ($= r_{\mathrm{p}}v_{\mathrm{i}}^{\mu}\delta^{\nu}$), and they are $b = -\mu/(2+\mu)$ and $c = (2+\mu-6\nu)/3(2+\mu)$. For simplicity, the terms on Equation 1 are rewritten using the following nondimensional parameters: $\pi_{\mathrm{R}} = R\left(\rho_{\mathrm{b}}/m_{\mathrm{p}}\right)^{1/3}$, $\pi_2 = gr_{\mathrm{p}}/v_{\mathrm{i}}^2$, and $\pi_4 = \rho_{\mathrm{b}}/\delta$. The parameters H_1, b, and c are determined for each target in our experiments. R is the crater radius: it was calculated from the measured value of R_{rim} and the ratio, R_{rim}/R, as shown on Section 3.1 and Table 1. At high impact velocity (>1.1 km s^{-1}), the R_{rim}/R for the 0.1 mm target and part of the Mix F without "C-10" targets was used the measured value of the laser displacement meter. However, the R_{rim}/R for the rest of the Mix F and "C-10" targets could not be determined due to the ambiguous crater profiles (Figure S2 in Supporting Information S1). In these cases, the averaged R_{rim}/R value measured for the Mix F without "C-10" targets was used. At low impact velocity (<210 m s^{-1}), the crater profiles were not measured by the laser displacement meter, so the R_{rim}/R was not determined directly. Then, the averaged R_{rim}/R value of the 0.1 mm target and the Mix F without "C-10" targets obtained at high impact velocity was used for each target. In the case of the Mix T and "C-10" targets, the averaged R_{rim}/R value of the Mix F without "C-10" targets at high impact velocity was used.

Figure 4a shows the relationship between the π_{R} and the π_4 at constant π_2, in which the π_2 is $(4.3\text{–}4.9) \times 10^{-7}$ for low velocity (<210 m s^{-1}), and $(2.5\text{–}3.2) \times 10^{-10}$ for high velocity (1.1–4.4 km s^{-1}). From this figure, we can obtain the parameter c for Equation 1. But the data for the 0.1 mm target were not sufficient to determine the c in both impact velocity ranges, so we determined the c from the data for the Mix F: It was 0.023 ± 0.016 for low velocity, and 0 for high velocity.

Figures 4b and 4c show the relationship between the π_{R} normalized by the π_4^c and the π_2 for all data. The parameter c for the 0.1 mm target and the Mix T was not determined in this study. Therefore, it was assumed that the c of the 0.1 mm target was the same as that of 0.2 mm-sized glass beads obtained by Yasui et al. (2015) whereas the c of the Mix T was assumed to be the same as that of the Mix F without "C-10" targets determined in the low and high impact velocity ranges, respectively. At π_2 values greater than 3×10^{-7} (low velocity) shown in Figure 4c, the π_{R}/π_4^c for 0.1 mm target is clearly separated from that for the Mix T and F, and it is about 20% larger. This is because the angle of repose for the Mix T and F is larger than that for the 0.1 mm target, so the friction among the beads reduces the crater size for the Mix T and F (Uehara et al., 2003; Wünnemann et al., 2010). The π_{R}/π_4^c for the Mix T is positioned at the upper part where the π_{R}/π_4^c for the Mix F is distributed. On the other hand, in the "C-10" Mix T and F, the projectile collides with the 10 mm-sized target bead, and the π_{R}/π_4^c is positioned at the lower part. From these results, we speculated a first contacted position of the projectile to collide with the Mix T and F in three different patterns. Figures 4d and 4e shows a schematic illustration of the arrangement of target beads and potential impact points (patterns 1–3) for the Mix T (Figure 4d) and Mix F (Figure 4e) illustrated from the above speculation; they are not depiction that was directly observed from a particular experiment. In the case of the "C-10" Mix T and F, the impact point is shown as pattern 1. Thus, the π_{R}/π_4^c distributed in the upper part could be originated from the collisions between the projectile and a 1 or 3 mm-sized target bead for the Mix T (pattern 2 on Figure 4d). According to this speculation, the π_{R}/π_4^c distributed at the upper part for the Mix F could also be explained by the collisions of a 1 or 3 mm-sized target bead (pattern 2 on Figure 4e).

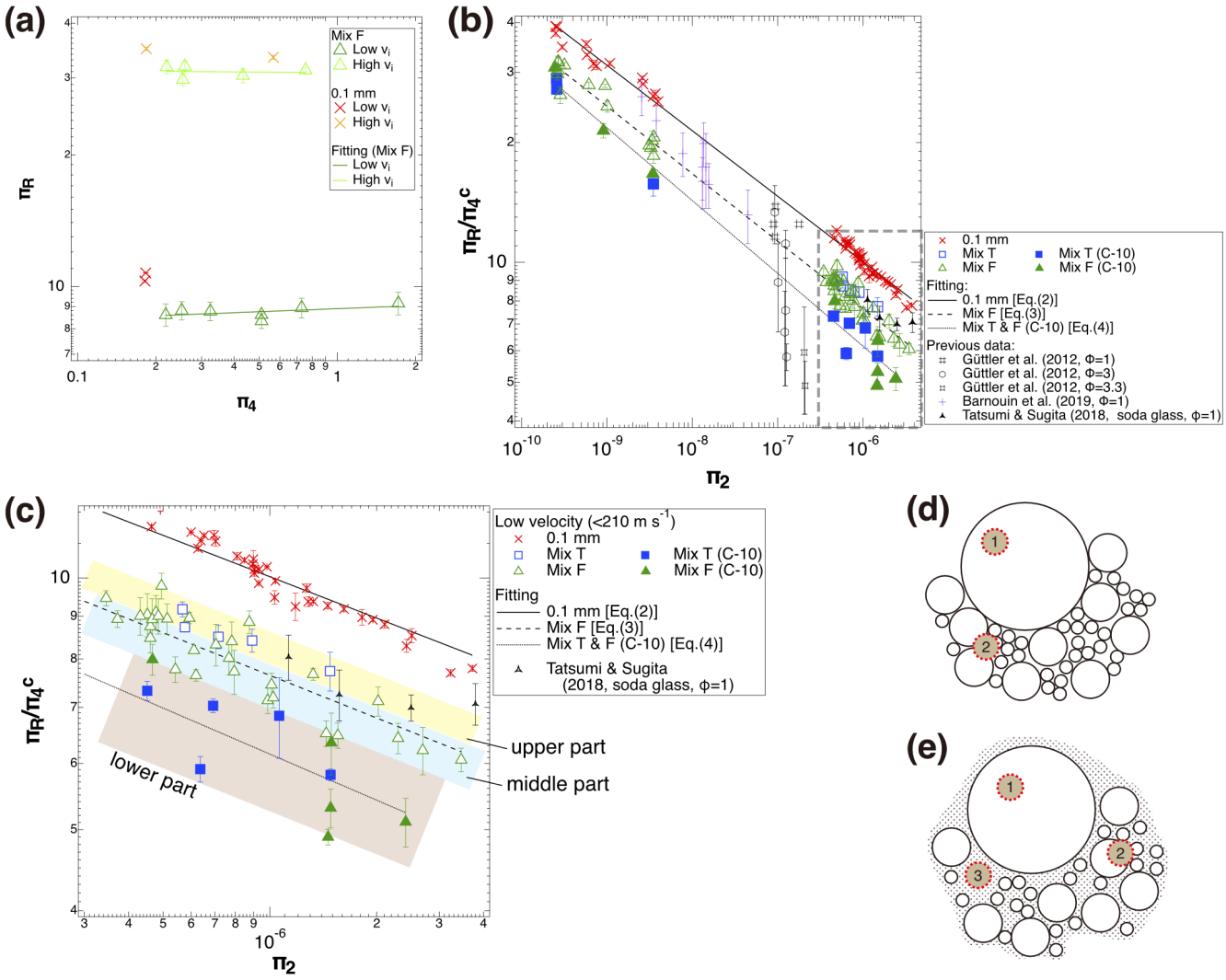

Figure 4. (a) Relationship between the π_R and the π_4 at constant π_2. "Low v_i" means an impact velocity smaller than 210 m s^{-1}, and "High v_i" means 1.1–4.4 km s^{-1}. The two solid lines for the Mix F are the fitting lines for each velocity range that were used to obtain the parameter c on Equation 1. (b) Relationship between the π_R normalized by the π_4^c and the π_2 for all shots. The three lines are the fitting lines for each target; they correspond to Equations 2–4. (c) An enlargement of the area surrounded by the dashed line on panel (b). The enlarged area showing the Mix T and F results is divided into three colored areas explained in Section 3.2. (d) (e) Schematic illustrations of the first contacted position depending on the target bead for the (d) Mix T and (e) Mix F speculated from the panel (c). The black circles show the target bead; the largest is a 10 mm-sized bead and the smallest is 1 mm-sized bead. The dotted region in panel (e) represents the pool of 0.1 mm-sized beads. The dotted red circles indicate the first contacted position of the projectile (patterns 1–3).

In addition, there are values positioned at the middle part of the π_R/π_4^c for a Mix F located between the values for a Mix T and that for a "C-10" target. These could have originated from the collisions between the projectile and the pool consisting of 0.1 mm-sized beads at the first contact (pattern 3 on Figure 4e).

When the π_2 was smaller than 3×10^{-9} (high velocity), the π_R/π_4^c values for the Mix F approached that for the "C-10" Mix T and F, and they almost matched each other at $\pi_2 = 3 \times 10^{-10}$. In this π_2 range, we recovered the projectile and the target beads disrupted into fragments after a shot. So the region around the impact point was expected to be composed of comminuted fragments.

The π_R/π_4^c results for the 0.1 mm target and Mix F are approximated using the crater size scaling law, Equation 1, by the least squares method for all ranges of the π_2 as follows:

$$\pi_R/\pi_4^c = 10^{0.01\pm0.01}\pi_2^{-0.16\pm0.002} \quad (0.1 \text{ mm target}), \tag{2}$$

$$\pi_R/\pi_4^c = 10^{-0.13\pm0.02}\pi_2^{-0.17\pm0.003} \text{ (Mix F)}, \quad (3)$$

where Equation 3 does not include the "C-10" results. Although the results of patterns 2 and 3 for the Mix F in Figures 4d and 4e are slightly separated from each other in Figure 4c, Equation 3 used both results to obtain the scaling relationship in the ϕ range of 0.03–3. In this study, the Mix T showed all "C-10" when π_2 was smaller than 3×10^{-10}. Therefore, the original scaling relationship for the Mix T without "C-10" results was not obtained.

On the other hand, the π_R/π_4^c for both the "C-10" Mix T and the "C-10" Mix F is smaller than those of the 0.1 mm target or these mixed targets without "C-10" results. As is the case for the 0.1 mm target and Mix F without "C-10" results, the crater size scaling relationship for the "C-10" Mix T and F is approximated as follows:

$$\pi_R/\pi_4{}^c = 10^{-0.31\pm0.05}\pi_2{}^{-0.18\pm0.01} \text{ ("C} - \text{10" Mix T and F)}, \quad (4)$$

And the c values of the Mix F without "C-10" results at low and high impact velocity ranges were used in Equation 4.

From Equations 2–4, the exponents of a coupling parameter, μ and ν, were calculated as 0.39 ± 0.01 and 0.32 ± 0.001 for the 0.1 mm target, 0.41 ± 0.01 and 0.38 ± 0.02 for the Mix F without "C-10" results, and 0.45 ± 0.02 and 0.39 ± 0.03 for the "C-10" Mix T and F. The μ for the 0.1 mm target is the smallest, and it is slightly smaller than that of loose sand determined by Housen and Holsapple (2011) (0.41), but the μ for the Mix F without "C-10" targets matched well with that of loose sand. On the other hand, the μ for the "C-10" Mix T and F is the largest one. The ν values for the Mix targets (the Mix F without "C-10" results and the "C-10" Mix T and F) were about 0.38, and it is larger than that for the 0.1 mm target, but this was almost identical to the typical value of 0.4 proposed by Housen and Holsapple (2011).

Next, we compared our results to the previously reported results for glass beads with ϕ of ≥ 1 (Barnouin et al., 2019; Güttler et al., 2012; Tatsumi & Sugita, 2018) as shown in Figures 4b and 4c. The materials and sizes of the projectile and target grains used in these previous studies are summarized in Table S1 in Supporting Information S1, for comparison with those used in this study. These previous data could be classified into an armoring regime I proposed by Tatsumi and Sugita (2018), in which the ϕ is larger than 1 and the ξ showing the kinetic energy of the projectile normalized by the energy required to disrupt the first contacted target bead is larger than 1. The results of $\phi = 1$ in these previous studies are smaller than the results of $\phi \leq 0.1$ for our 0.1 mm target. According to their scaling relationship of spherical glass beads (Equation 9 in Tatsumi & Sugita, 2018), the armoring effect is negligibly small for our 0.1 mm target. On the other hand, the crater size of $\phi = 1$ calculated using Tatsumi's scaling relationship reduces 5% due to the armoring effect compared with that for our 0.1 mm target but the previous experimental results (Barnouin et al., 2019; Güttler et al., 2012; Tatsumi & Sugita, 2018) are slightly smaller than these calculated results. Moreover, the calculated crater size of $\phi = 3$ using Tatsumi's scaling relationship reduces 20% while the experimental results of Güttler et al. (2012) are much smaller. We will improve their model to resolve this small inconsistency.

In the case of constant projectile density (e.g., in the case of a SUS projectile), Equation 1 is described by using the kinetic energy of the projectile, E_k, and thus can be rewritten as $R \propto r_p^{4b+1} E_k^{-b}$. The value of b is determined to be -0.17 for the 0.1 mm target on Equation 2 and -0.18 for the Mix F without "C-10" results on Equation 3, respectively. So the powers of the $r_p$and E_k are $4b + 1 = 0.28$–0.32 and $-b = 0.17$–0.18, respectively. Thus, their powers are almost consistent with $\alpha = 0.35 \pm 0.06$ and $\gamma = 0.17$–0.18 on the last paragraph of Section 3.2. This is the reason why the crater rim diameter, D_{rim}, can be scaled by $r_p^{\alpha} E_k^{\gamma}$ for each target as shown in Figure 3d.

4. Discussion

Tatsumi and Sugita (2018) proposed two armoring regimes classified by ϕ and ξ: they are armoring regime I at $\phi > 1$ and $\xi \gtrsim 1$, and armoring regime II at $\phi > 1$ and $\xi < 1$. They proposed a crater scaling relationship of armoring regime I using ϕ and ξ. In armoring regime II, only the first contacted target grains were disrupted and no impact craters were clearly formed. So they did not discuss the scaling relationship of armoring regime II. In this study, we identified the impact crater even in armoring regime II. This result appears to be a unique phenomenon in granular targets with a size frequency distribution.

One of the most important results in our experiments is that the cratering efficiency of the "C-10" Mix T and F was smaller than that for the Mix F without "C-10" results. We calculated the ξ of the "C-10" targets using the impact strength of glass sphere obtained by Yasui et al. (2020) (in this calculation, we assumed that the impact strength did not depend on size), and compared them with the appearance of the recovered fragments of impacted 10 mm-sized glass bead or itself. As a result, the impacted 10 mm-sized bead was cracked at $\xi = 0.05$–1.3 or disrupted into some fragments at $\xi = 2.0$–27.8. According to Tatsumi's definition of the armoring regime, our "C-10" Mix T and F results fall into armoring regimes I and II, depending on the impact velocity. Here, we improved the scaling relationship of armoring regime I proposed by Tatsumi and Sugita (2018) to be applicable to targets with a power-law bead size distribution and applied this improved relationship to a cratering efficiency in armoring regime II.

To develop a scaling relationship for "C-10" targets, we assume that the momentum of the projectile is transferred to a first contacted 10 mm-sized bead, and the contacted bead is accelerated and collides with the neighboring beads surrounding it, which is similar to the model proposed by Güttler et al. (2012) and Tatsumi and Sugita (2018). Then, we introduce the reduction rate of the cratering efficiency to Equation 1 and construct the improved Equation 1 in order to accurately reproduce the experimental results for the case of a "C-10" target. In this model, the parameters related to the projectile on Equation 1 are replaced with those related to the first contacted 10 mm-sized glass bead as follows:

$$R\left(\frac{\rho_b}{m_t}\right)^{\frac{1}{3}} = H_1\left(\frac{g r_t}{v_t^2}\right)^b \left(\frac{\rho_b}{\rho_t}\right)^c, \tag{5}$$

where m_t, r_t, and ρ_t are the mass, radius, and density of the first contacted glass bead, respectively, and v_t is the colliding velocity of the first contacted bead with its neighbors. The parameters, b and c, are constant, as same as Equation 1. Güttler et al. (2012) and Tatsumi and Sugita (2018) consequently used the velocity of the center of mass as the colliding velocity because they considered that the effect of the restitution coefficient was negligibly small relative to the colliding velocity. Holsapple and Housen (2012) and Housen and Holsapple (2015) showed that the momentum transfer efficiency, β, was 1 for a perfectly inelastic collision, but that β increased beyond 5 for cohesive rock due to the mass and the velocity of ejecta in high velocity collisions. The β is defined as $m_t v_t / m_p v_i$, so $v_t = \beta m_p v_i / m_t$. Equation 5 is rewritten by using the non-dimensional scaling parameters, π_R, π_2, and π_4, and the β, and the improved crater size scaling relationship is shown as follows:

$$\pi_R = H_1 \pi_2^b \pi_4^c \beta^{-2b} \left(\frac{m_t}{m_p}\right)^{\frac{1}{3}+2b-c} \left(\frac{r_t}{r_p}\right)^{b+3c} = f(\phi) H_1 \pi_2^b \pi_4^c \tag{6}$$

Here, we used $\phi = r_t / r_p$ and assumed that the projectile and the first contacted bead had a perfect sphere, so the reduction factor of the cratering efficiency, $f(\phi)$, is written as follows:

$$f(\phi) = \beta^{-2b} \left(\frac{\rho_t}{\delta}\right)^{\frac{1}{3}+2b-c} \phi^{1+7b} \tag{7}$$

Here, we use Equation 7 for our "C-10" targets, so a radius of the first contacted bead, r_p, is 5 mm (in this case, ϕ was defined as ϕ_{10}). In the later discussion, we applied Equation 7 to various target particles that were larger than the impactor size. The $f(\phi) = 1$ in Equation 6 merges with the crater scaling relationship of the Mix F without "C-10" results shown by Equation 3. As the $f(\phi)$ must be smaller than 1, Equation 7 is used at $\phi \geq \left[\beta^{-2b} (\rho_t / \delta)^{1/3+2b-c}\right]^{-1/(1+7b)}$. We used our scaling parameters, H_1, b, and c of Equation 3 in Equation 6, and calculated the $f(\phi)$ for our experimental "C-10" Mix T and F results. Then, we obtained the β necessary for reproducing the calculated $f(\phi)$ using Equation 7.

Figures 5a and 5b shows the relationship between the ϕ_{10} and the π_R normalized by $H_1 \pi_2^b \pi_4^c$. The π_R normalized by $H_1 \pi_2^b \pi_4^c$ corresponds to the $f(\phi)$, so the experimental results for the "C-10" targets can be compared with the Equation 7 to determine the β. In order to calculate the $f(\phi)$, the parameters H_1 and b in Equation 6 were used as the values of Equation 3 and the value of c was taken as the average value, 0.012, at both impact velocity ranges. The curves are calculated by Equation 7 with different values of β ranging from 1 to 4 for each projectile type. The upper limit of Equation 7 is equal to that of Equation 3 in this model. The curve of $\beta = 1$ means a perfectly inelastic collision (Housen & Holsapple, 2015). Most of the results for the "C-10" targets are between the upper

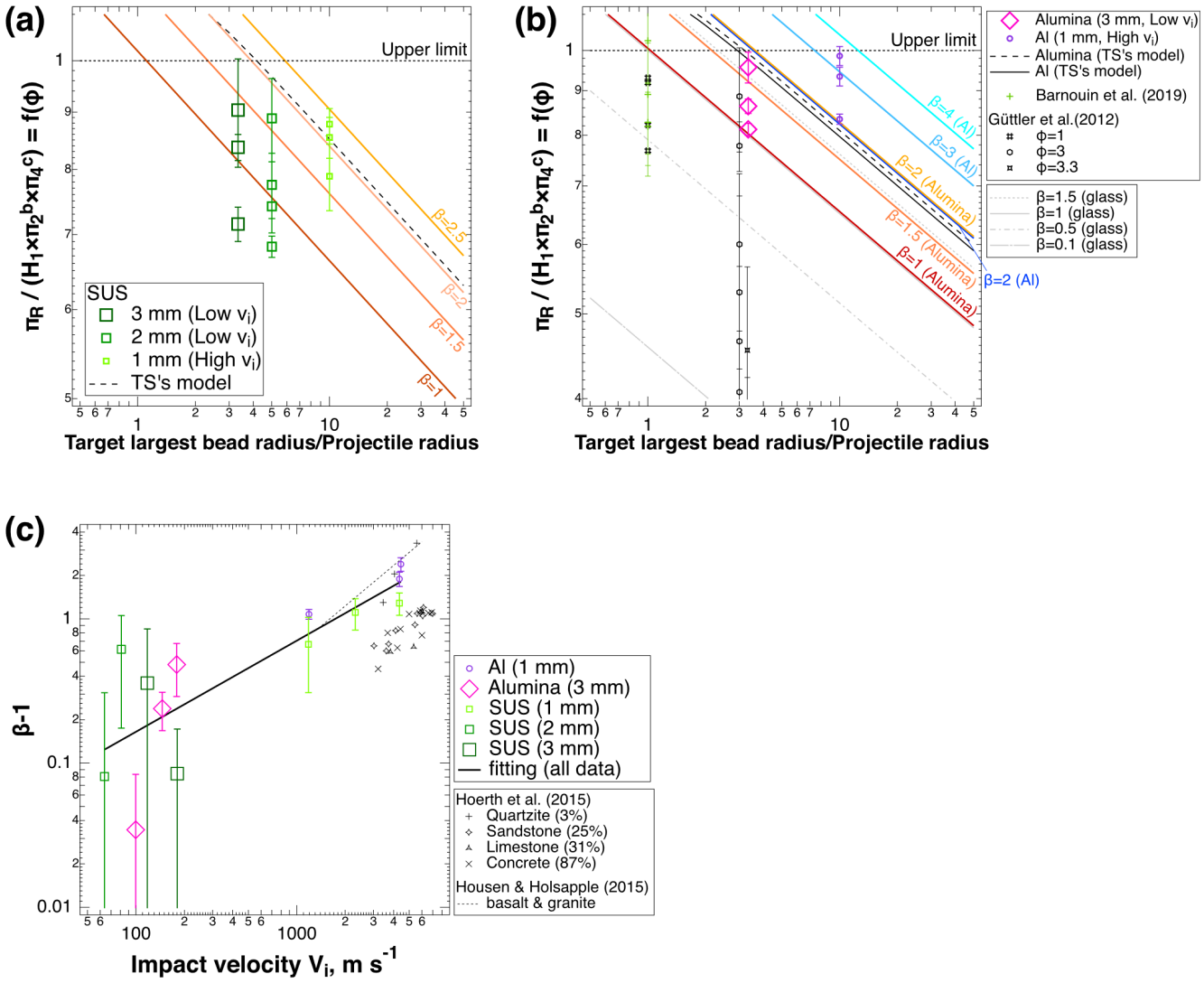

Figure 5. Relationship between the π_R normalized by $H_1\pi_2^b\pi_4^c$ and the ratio of the target with the largest bead radius to the projectile radius for (a) SUS projectiles with diameters of 2 and 3 mm at low impact velocity range and a diameter of 1 mm at high impact velocity range, and (b) an Al_2O_3 projectile with a diameter of 3 mm at low impact velocity range and an Al projectile with a diameter of 1 mm at high impact velocity range. The plots show the experimental results for the "C-10" targets. The colored lines show the $f(\phi)$ of Equation 7 at constant β, from 1 to 4, for each projectile type, with $\beta = 1$ being the lower limit. The dotted line is the upper limit of $f(\phi)$: the armoring is not effective at $f(\phi) \geq 1$. The experimental results of Güttler et al. (2012) and Barnouin et al. (2019), and the four gray lines for a glass projectile calculated using Equation 7 changed β from 0.1 to 1.5 are also shown on panel (b). The black lines show the $f(\phi)$ of the model proposed by Tatsumi and Sugita (2018) (TS's model) for each projectile type. (c) Relationship between the $\beta - 1$ and the impact velocity for the "C-10" targets determined from panels (a) and (b). The solid line is the fitting line of Equation 8. The dotted line shows the results of non porous rocks obtained by Housen and Holsapple (2015).

limit and the line of $\beta = 1$ although a few data are below this line. According to this figure, the momentum transfer efficiency, β, is estimated to be 1–1.5 at low velocity range and 1.5–3.5 at high velocity range: β increases with increasing impact velocity.

It was unexpected that three experimental results for a SUS projectile with a diameter of 2 or 3 mm were smaller than the curve of $\beta = 1$. This might have been due to the initial arrangement of 10 mm-sized beads on the target surface: The concentration of 10 mm-sized beads might have been higher than that of the other-sized beads, and this could have reduced the cratering efficiency.

Tatsumi and Sugita (2018) proposed a crater volume scaling relationship including the armoring effect for a target composed of particles of a single size. Their proposed scaling relationship for smooth spherical particles can be compared with our improved scaling relationship for a Mix F. The reduction factor of the cratering effi-

ciency, $f(\phi)$, is obtained for the model of Tatsumi and Sugita by transforming Equations 8 and 9 of Tatsumi and Sugita (2018), as $f(\phi) = (5.7/\pi)^{1/3}\left[1 + \phi^3\,(\rho_t/\delta)\right]^{-2(3\mu-1)/3(2+\mu)}$, where the crater volume is approximated by the cone shape. The reduction factor of Tatsumi and Sugita (2018) is close to the relationship of $\beta = 1.5$–2 in our model, but not sufficiently close to fit all of our experimental results. Though the dependence of the ϕ on the reduction factor in Equation 7 is similar to that in the above equation, $f(\phi) = (5.7/\pi)^{1/3}\left[1 + \phi^3\,(\rho_t/\delta)\right]^{-2(3\mu-1)/3(2+\mu)}$, of Tatsumi and Sugita (2018), our model can predict various reduction factors at constant ϕ by using β, and it can explain the experimental data.

Using the same method, the β values of Güttler et al. (2012) and Barnouin et al. (2019) were calculated and shown in Figure 5b. The $f(\phi)$ of Güttler et al. (2012) was calculated by normalizing each π_R value of $\phi \geq 1$ with their mean π_R of $\phi < 1$. The $f(\phi)$ of Barnouin et al. (2019) was calculated by normalizing each π_R value of $\phi = 1$ with the π_R calculated using Equation 2 for our 0.1 mm target. Their β values were smaller than our results: they were 0.5–1 for $\phi = 1$, 0.2–1.5 for $\phi = 3$, and ~0.2 for $\phi = 3.3$. This means that the armoring effect is more efficient for equal-sized granular targets. This can be seen as a difference in a crater formation process of armoring regime II. That is, craters were not clearly formed in equal-sized granular targets whereas they were clearly formed in our targets with size frequency distribution. Thus, the difference between our model and Tatsumi's model is that the degree of armoring effect on cratering efficiency appears in β.

Figure 5c shows the impact velocity dependence of $\beta - 1$ obtained from Figures 5a and 5b for a "C-10" target. We can say that the $\beta - 1$ increases with increasing impact velocity, irrespective of the projectile type, although the data is somewhat scattered and the error is larger at low impact velocity range. This relationship is fitted by the one power-law equation as follows:

$$\beta - 1 = 10^{-2.05\pm0.38}\,v_i^{0.63\pm0.14} \tag{8}$$

This relationship is very similar to those of rocks with a porosity of <3%, but larger than those for porous rocks as shown in the figure (Hoerth et al., 2015; Housen & Holsapple, 2015). Thus, the β could depend on a porosity as mentioned in previous studies (Flynn et al., 2020; Holsapple & Housen, 2012).

Holsapple and Housen (2012) and Jutzi and Michel (2014) showed that the $\beta - 1$ was proportional to $\left(v_i/\sqrt{Y_t/\rho_t}\right)^{3\mu_s-1}$, where Y_t is the static strength of target, and μ_s is the exponent of a coupling parameter of π-scaling law in the strength-dominated regime. The power-law relationship of v_i on Equation 8 follows the relationship of $(\beta - 1) \propto v_i^{3\mu_s-1}$. Applying our result to this model, the μ_s is calculated to be 0.54, and it is almost consistent with that of rock (0.55) obtained by Housen and Holsapple (2011). Moreover, the $\beta - 1$ depends on the strength, Y_t, in their model, so our improved crater scaling relationship includes the strength-related term in $\beta - 1$ as a specific velocity, $\sqrt{Y_t/\rho_t}$. Thus, the reduction factor including the β in Equation 7 depends on the strength of a first contacted bead even when the target has no bulk strength or in the gravity regime.

By substituting Equations 7 and 8 into Equation 6, the improved crater scaling relationship including the armoring effect is obtained as follows:

$$\pi_R/\pi_4^c = H_1\left[1 + \left(8.99\times10^{-3}\right)v_i^{0.63}\right]^{-2b}\left(\frac{\rho_t}{\delta}\right)^{\frac{1}{3}+2b-c}\phi^{1+7b}\pi_2^b \tag{9}$$

In this study, we obtained $b = -0.17$ and $c = 0.012$ (the averages of the low and high velocity ranges) for the Mix F without "C-10" results. Accordingly, the power law index of ρ_t/δ in Equation 9 is −0.0097, so this term is almost unity. Thus, we can calculate the crater size with consideration for the armoring effect according to Equation 9, and our "C-10" data are reproduced by this equation with different ρ_t/δ and ϕ of the first bead contacted by the projectile (in this case, we consider only the "C-10" data, so $\phi = \phi_{10}$). Figure 6 shows the relationship between the π_R/π_4^c and the π_2 for a "C-10" target at constant surface gravity: The impact velocity, v_i, is only changed from 5,000 to 10 m s^{-1} in π_2. This figure shows the same results as in Figure 4b, but the "C-10" data are grouped according to ϕ_{10}, 3.3, 5, and 10. Most of experimental data for each grouped ϕ_{10} are on the lines calculated from Equation 9, although some are off from the calculated lines, especially in the low impact velocity range. As π_2 decreases, the improved scaling relationship of Equation 9 at constant surface gravity merges with Equation 3; that is, $f(\phi) = 1$. At a π_2 smaller than that at $f(\phi) = 1$, the crater size follows Equation 3. The π_2 at

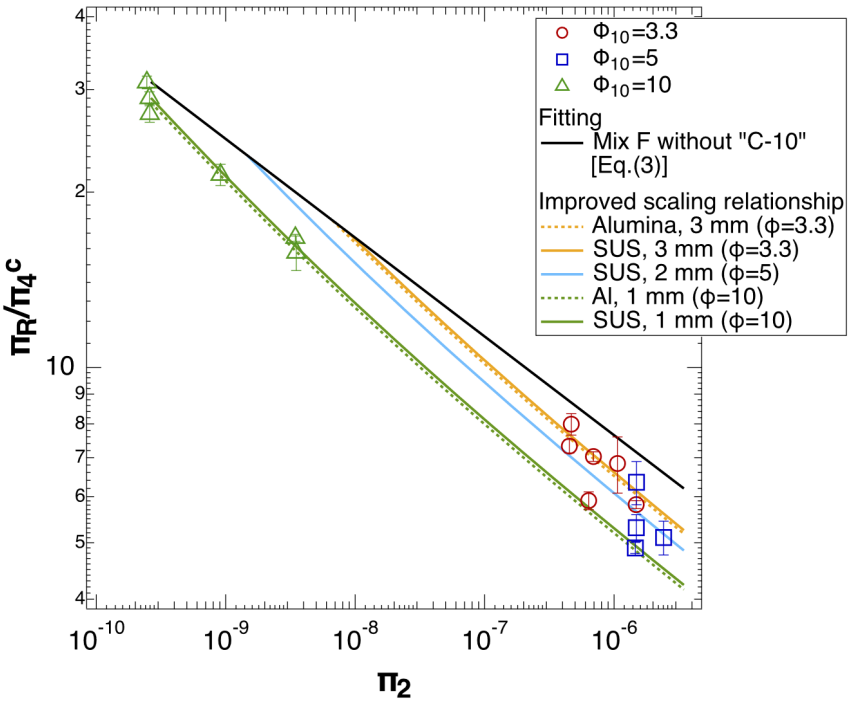

Figure 6. The experimental results from Figure 4b for the "C-10" targets with $\phi_{10} = 3.3$, 5, and 10. The black solid line shows the crater size scaling relationship for the Mix F without "C-10" results shown by Equation 3. The colored lines show the calculated results of Equation 9 for various projectile types (the size in the legend corresponds to the projectile diameter).

$f(\phi) = 1$ decreases with increasing ϕ at constant surface gravity, as shown in Figure 6, and the impact velocity corresponding to $f(\phi) = 1$ is shown as follows:

$$v_i \geq \left[\frac{\left\{ (\rho_t/\delta)^{1/3+2b-c} \phi^{1+7b} \right\}^{1/2b} - 1}{8.99 \times 10^{-3}} \right]^{1/0.63} \quad (10)$$

Equation 10 thus represents the impact condition without an armoring effect.

The π_2 depends on not only the impact velocity but also the surface gravity. The improved scaling relationship can also be plotted by changing surface gravity at constant impact velocity. Figure 7a shows the armoring effect on the crater scaling relationship plotted by changing the surface gravity at constant impact velocity, as shown by the solid lines. The parameters r_p, v_i, and δ are referenced from the SCI impact experiment from the Hayabusa2 mission to asteroid Ryugu (Arakawa et al., 2020), and the ρ_b is assumed to be the average density of Ryugu (Watanabe et al., 2019). The calculated lines of ϕ =10, 100, and 500 are parallel to that without an armoring effect, and the armoring effect is enhanced with increasing ϕ. For example, if the SCI is assumed to collide with a boulder with a diameter of 13 m ($\phi = 100$, blue colored circle in Figure 7a), the crater size could be reduced to half of that without an armoring effect. But if the boulder impacted by SCI was smaller than 52 cm ($\phi < 4.0$), the crater size could not be affected by the first contacted boulder. Arakawa et al. (2020) concluded that the diameter of the SCI crater was almost the same as the estimate from the crater size scaling law of loose sand in the gravity regime (Housen & Holsapple, 2011). This means that the armoring effect was small enough to be approximated by a scaling law for a target with homogeneous particles of a single size. This phenomenon might have been caused by the reduction factor, $f(\phi) = 1$; that is, the first contacted boulder impacted by the SCI impactor might be smaller than 52 cm.

The dashed lines show the scaling relationship plotted by changing the impact velocity under a constant surface gravity for Ryugu (1.2×10^{-4} m s^{-2}): More specifically, they show the crater size when the SCI impactor collided with a boulder (first contacted boulder) of diameter 1.3, 13, or 65 m (ϕ = 10, 100, and 500, respectively) at an impact velocity of 10 km s^{-1} to 10 m s^{-1}. At a wide range of ϕ, the armoring effect is reduced with increasing v_i,

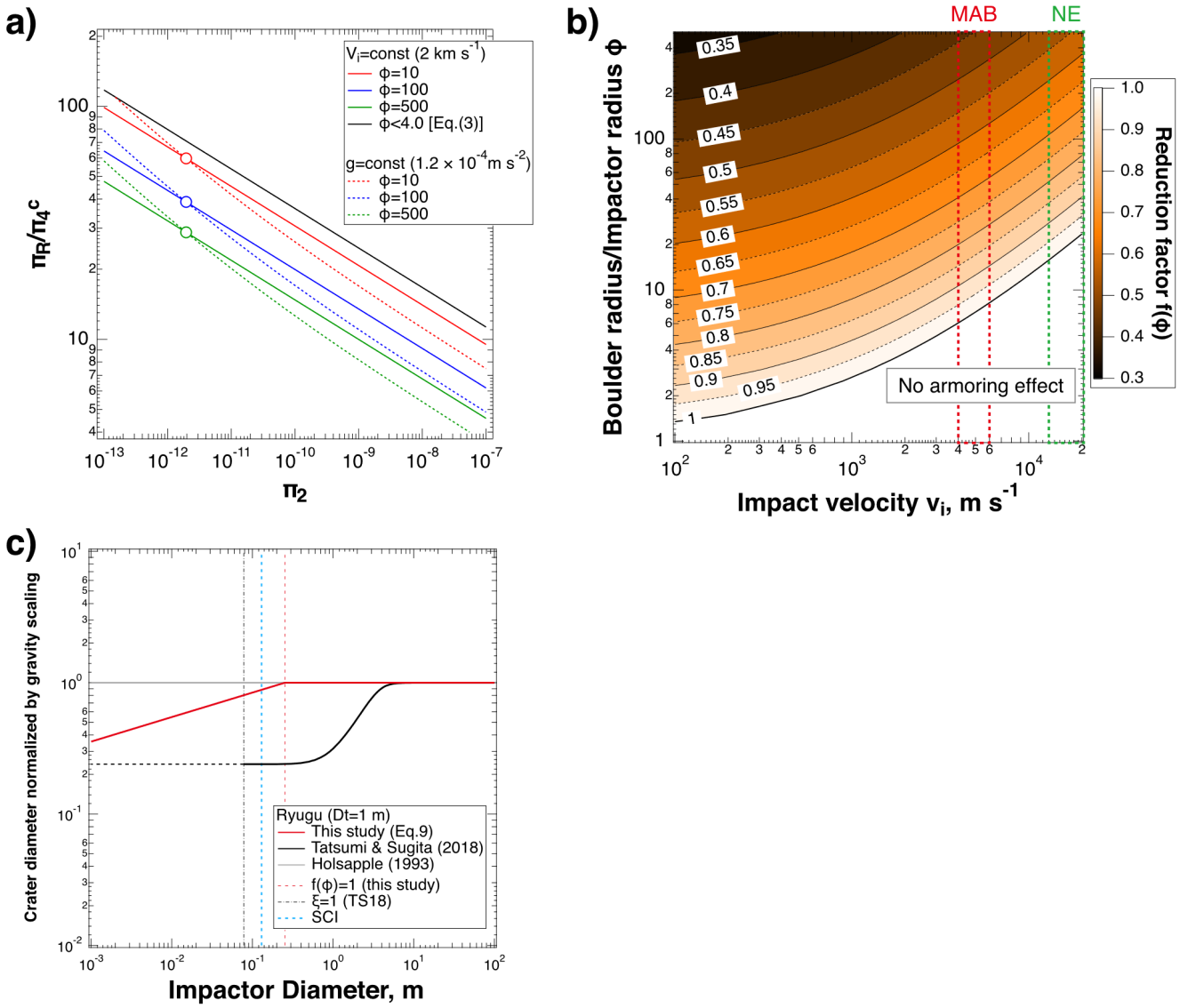

Figure 7. (a) Calculated results of Equation 9 plotted by changing the impact velocity (dotted lines) and the surface gravity (solid lines) on the relationship between the π_R/π_4^c and the π_2. The three colored open circles show the impact condition for the SCI impactor impacting Ryugu. (b) Contour map of the reduction factor, $f(\phi)$, changing with the impact velocity, v_i, and the size ratio of the (first contacted) boulder size to the impactor, ϕ, in 0.05 increments. The color bar shows the magnitude of the reduction factor, $f(\phi)$. The rectangular region surrounded by the red and green lines show the collisional velocity range in the main asteroid belt (MAB, Bottke et al., 1994) and near-Earth space environment (NE, Moorhead, 2018), respectively. (c) Calculated crater diameter for collisions between the first contacted boulder with the diameter of 1 m and various sized impactors on Ryugu. The red line shows our scaling relationship of Equation 9. The black line (including the black horizontal dashed line) shows the scaling relationship of Tatsumi and Sugita (2018) for angular shaped target grains. The gray line shows the gravity scaling law of Holsapple (1993) for dry sand. The vertical red dotted line shows the $f(\phi) = 1$ of this study. The vertical black dotted line shows the lower limit of crater size estimated by Tatsumi's model ($\xi = 1$). The vertical blue dotted line shows the SCI impactor diameter (Arakawa et al., 2020).

but the reduction factor, $f(\phi)$, is smaller with increasing ϕ. Figure 7b shows the contour map of the $f(\phi)$ changing with the impact velocity and the ϕ. At the region below the line of $f(\phi) = 1$, the armoring effect does not function, and this region expands toward large ϕ with increasing v_i. At constant ϕ, the reduction factor approaches unity as the impact velocity increases, as already shown in Figures 6 and 7a. At the average collisional velocity in the main asteroid belt (4–6 km s^{-1}, Bottke et al., 1994), the armoring effect on the crater formation could function on the surface covered with boulders having a size distribution in which the size of the impacted boulder is >6–8 times larger than the size of the impactor. The average collisional velocity in the near-Earth space environment is 13–20 km s^{-1} (Moorhead, 2018), so the armoring effect could function at the size ratio of the impacted boulder to the impactor >16. Figure 7b enables us to estimate the $f(\phi)$ for the impactor collision on the first contacted

boulder with various ϕ values at various v_i. Therefore, our improved crater size scaling relationship including the armoring effect will help to refine the crater chronology on rubble-pile asteroids covered with boulders of various sizes, such as Ryugu, through reconstruction of the crater size frequency distribution.

The returned samples from Ryugu by Hayabusa2 revealed that they had a high microporosity, ~46% (Yada et al., 2022) although our improved scaling relationship is based on the results of granular targets made of glass beads without microporosity, and it does not explicitly describe the effect of micropores on Ryugu's boulders. However, Housen et al. (2018) showed that the compaction of micropores dominated the cratering formation processes only at π_2 greater than 10^{-6} and that the cratering process was mainly controlled by the gravity even for the granular targets made of grains with micropores at π_2 smaller than 10^{-6}. Since the SCI impact and other collisions on Ryugu were done at π_2 smaller than 10^{-10}, the cratering on Ryugu may be dominated only by the gravity. This means that our improved scaling relationship, which includes the effects of boulder size and strength, could be applied to collisional phenomena on Ryugu and other small asteroids.

Finally, we compare our scaling relationship of Equation 9 with Tatsumi and Sugita's model: Their models are calculated to show the relationship between the impactor size and the crater size on Ryugu. This relationship is essential for estimating the crater retention age of asteroids. Figure 7c shows a predicted crater diameter on Ryugu for various sized impactors colliding with boulder with the diameter of 1 m. This is similar to Figure 17b in Tatsumi and Sugita (2018), but in this figure the SCI impact on Ryugu was calculated by using the bulk density and the impact velocity of SCI impactor of $\delta = 1{,}740$ kg m^{-3} and $v_i = 2{,}000$ m s^{-1} (Arakawa et al., 2020), the bulk density of boulder of $\rho_t = 1{,}282$ kg m^{-3} (Yada et al., 2022), and the surface gravity of $g = 1.2 \times 10^{-4}$ m s^{-2} (Watanabe et al., 2019). Tatsumi's result for π_R is normalized by π_R calculated by π-scaling law in the gravity-dominated regime for dry sand (e.g., Holsapple, 1993) whereas our result for π_R is normalized by our scaling relationship for the Mix F without "C-10" results in Equation 3 under the same impact conditions. In the case of our model, the crater diameter decreases due to the armoring effect at $f(\phi) < 1$. The upper limit of the impactor diameter which can reduce the crater diameter is 25 cm: It is 1/4 of the impacted boulder of 1 m and twice of the SCI impactor size of 13 cm. On the other hand, in Tatsumi's model, the reduction of crater diameter due to the armoring effect occurs even for the impactors with the diameter of ~8 m, which is much larger than the upper limit of our model. Moreover, in their model, the armoring effect is maximized at the impactor diameter of 30 cm, and the reduced crater diameter is unchanged even at the impactor size smaller than 30 cm. Tatsumi's model can be applied to asteroids whose surface is covered with equal-sized boulders (e.g., 1 m in diameter), and the armoring effect is rather strong compared to our model. This means that the impactor size >3 m is necessary for Tatsumi's model to reproduce the SCI crater of 14.5 m on Ryugu for the first contacted boulder with the diameter of 1 m. Since our model can be applied to asteroids whose surface is covered with boulders having a size frequency distribution, the SCI crater size is almost reproduced for the SCI impactor size of 13 cm. This means that our model predicts that the armoring effect is small for the SCI impact.

5. Conclusions

We conducted cratering experiments at impact velocities from 55 m s^{-1} to 4.4 km s^{-1} on various granular targets mixed with glass beads having the diameters of 0.1, 1, 3, and 10 mm, and the experiments were made for projectiles with various diameters and densities. In order to clarify the dependence of the size ratio, ϕ, of the first contacted target bead to the projectile on the armoring effect, the crater diameter was measured and the crater size scaling relationship was investigated. The results showed that the crater diameter formed on Mix F (including 0.1–10 mm-sized beads) was reduced by about 10–20% compared to that of 0.1 mm target when a first contacted bead was 0.1–3 mm in the diameter for a projectile with the diameter of 1–3 mm. The crater size scaling relationship for Mix F almost agrees with the previous results for $\phi = 1$ in Güttler et al. (2012), Tatsumi and Sugita (2018), and Barnouin et al. (2019). On the other hand, in Mix T (including 1–10 mm-sized beads) and F, when a first contacted bead was 10 mm in the diameter and the bead was cracked or disrupted ("C-10" target), the scaling diameter was clearly reduced: The crater diameter for the "C-10" target was reduced by 25–35% compared to that of the 0.1 mm target and by 20–25% compared to that of the Mix F without "C-10" results. While the crater size scaling relationship of the Mix F without "C-10" results well merged with that of the "C-10" target at the impact velocity increased at a constant gravity. These two relationships matched at a greater specific impact velocity as ϕ increased.

In order to reproduce the crater size of the "C-10" target, we introduced a reduction factor, $f(\phi)$, into the crater size scaling relationship for the Mix F without "C-10" results. Then, we constructed a scaling relationship that can be applied to the armoring regime II described by Tatsumi and Sugita (2018). It was found that the $f(\phi)$ was described by the momentum transfer efficiency, β, and the density ratio and size ratio of the first contacted target bead to the projectile. In addition, we found that the β increased with increasing impact velocity according to a power-law function, but no systematic changes were shown in the projectile size and density. Using our improved crater size scaling relationship including the $f(\phi)$, it is possible to predict the crater size on an asteroid covered with boulders of various sizes when a impactor collides at various impact velocities.

Data Availability Statement

Data used in Figures 3 and 4 are included in Table 1, and those used in Figures 2a and 2b, 3b–3d, 5, 6, 7a, Figures S1, and S2 in Supporting Information S1 are available in Yasui et al. (2022).

Acknowledgments

We appreciate the assistance of Mr. Y. Yamamoto and Mr. Y. Yokota of Kobe University in the performance of these experiments. We also thank Dr. M. Kiuchi and Dr. Y. Shimaki of the Institute of Space and Astronautical Science for their help with the experiments. Our series of experiments were supported in part by the Hypervelocity Impact Facility at ISAS/JAXA. This work was supported in part by a Grant-in-Aid for Scientific Research (no. 16K17794 to M. Yasui and no. 16H04041 and no. 17H06459 to M. Arakawa) from the Japan Society for the Promotion of Science (JSPS), and a Grant for a Joint Research Program.

References

Arakawa, M., Saiki, T., Wada, K., Ogawa, K., Kadono, T., Shirai, K., et al. (2020). An artificial impact on the asteroid (162173) Ryugu formed a crater in the gravity-dominated regime. *Science*, *368*(6486), 67–71. https://doi.org/10.1126/science.aaz1701

Arakawa, M., Wada, K., Saiki, T., Kadono, T., Takagi, Y., Shirai, K., et al. (2017). Scientific Objectives of small Carry-on impactor (SCI) and Deployable camera 3 digital (DCAM3-D): Observation of an ejecta curtain and a crater formed on the surface of Ryugu by an artificial high-velocity impact. *Space Science Reviews*, *208*(1-4), 187–212. https://doi.org/10.1007/s11214-016-0290-z

Barnouin, O. S., Daly, R. T., Cintala, M. J., & Crawford, D. A. (2019). Impacts into coarse-grained spheres at moderate impact velocities: Implications for cratering on asteroids and planets. *Icarus*, *325*, 67–83. https://doi.org/10.1016/j.icarus.2019.02.004

Bottke, W., Nolan, M., Greenberg, R., & Kolvoord, R. (1994). Velocity distribution among colliding asteroids. *Icarus*, *107*(2), 255–268. https://doi.org/10.1006/icar.1994.1021

Chapman, C. R., Merline, W. J., Thomas, P. C., Joseph, J., Cheng, A. F., & Izenberg, N. (2002). Impact history of Eros: Craters and boulders. *Icarus*, *155*(1), 104–118. https://doi.org/10.1006/icar.2001.6744

Flynn, G. J., Durda, D. D., Molesky, M. J., May, B. A., Congram, S. N., Loftus, C. K., et al. (2020). Momentum transfer in hypervelocity cratering of meteorites and meteorite analogs: Implications for orbital evolution and kinetic impact deflection of asteroids. *International Journal of Impact Engineering*, *136*, 193437. https://doi.org/10.1016/j.ijimpeng.2019.103437

Fujiwara, A., Kawaguchi, J., Yeomans, D. K., Abe, M., Mukai, T., Okada, T., et al. (2006). The rubble-pile asteroid Itokawa as observed by Hayabusa. *Science*, *312*(5778), 1330–1334. https://doi.org/10.1026/science.1125841

Gault, D. E., & Wedekind, J. A. (1978). Experimental studied of oblique impact. *Lunar and Planetary Science Conference*, *3*, 3843–3875.

Güttler, C., Hirata, N., & Nakamura, A. M. (2012). Cratering experiments on the self-armoring of coarse-grained granular targets. *Icarus*, *220*(2), 1040–1049. https://doi.org/10.1016/j.icarus.2012.06.041

Hirata, N., Barnouin-Jha, O. S., Honda, C., Nakamura, R., Miyramoto, H., Sasaki, S., et al. (2009). A survey of possible impact structures on 25143 Itokawa. *Icarus*, *200*(2), 486–502. https://doi.org/10.1016/j.icarus.2008.10.027

Hoerth, T., Schäfer, F., Hupfer, J., Millon, O., & Wickert, M. (2015). Momentum transfer in hypervelocity impact experiments on rock targets. *Process Engineering*, *103*, 197–204. https://doi.org/10.1016/j.proeng.2015.04.027

Holsapple, K. (1993). The scaling of impact processes in planetary sciences. *Annual Review of Earth and Planetary Sciences*, *21*(1), 333–373. https://doi.org/10.1146/annurev.ea.21.050193.002001

Holsapple, K., Giblin, I., Housen, K., Nakamura, A., & Ryan, E. (2002). Asteroid impacts: Laboratory experiments and scaling laws. In W. F. Bottke, A. Cellino, P. Paolicchi, & R. P. Binzel (Eds.), *Asteroid III* (pp. 443–462). University of Arizona Press.

Holsapple, K. A., & Housen, K. R. (2012). Momentum transfer in asteroid impacts. I. Theory and scaling. *Icarus*, *221*(2), 875–887. https://doi.org/10.1016/j.icarus.2012.09.022

Housen, K. R., & Holsapple, K. A. (2011). Impact cratering on porous asteroids. *Icarus*, *163*(1), 102–119. https://doi.org/10.1016/S0019-1035(03)00024-1

Housen, K. R., & Holsapple, K. A. (2015). Experimental measurements on momentum transfer in hypervelocity collisions. In *Proceedings of 46th lunar and planetary science conference 2015*, 2894

Housen, K. R., Schmidt, R. M., & Holsapple, K. A. (1983). Crater ejecta scaling laws: Fundamental forms based on dimensional analysis. *Journal of Geophysical Research*, *88*(B3), 2485–2499. https://doi.org/10.1029/JB088iB03p02485

Housen, K. R., Sweet, W. J., & Holsapple, K. A. (2018). Impacts into porous asteroid. *Icarus*, *300*, 72–96. https://doi.org/10.1016/j.icarus.2017.08.019

Jutzi, M., & Michel, P. (2014). Hypervelocity impacts on asteroids and momentum transfer I. Numerical simulations using porous targets. *Icarus*, *229*, 247–253. https://doi.org/10.1016/j.icarus.2013.11.020

Kadono, T., Suetsugu, R., Arakawa, D., Kasagi, Y., Nagayama, S., Suzuki, A. I., & Hasegawa, S. (2019). Pattern of impact-induced ejecta from granular targets with large inclusions. *The Astrophysical Journal Letters*, *880*(4), L30. https://doi.org/10.3847/2041-8213/ab303f

Lauretta, D. S., DellaGiustina, D. N., Bennett, C. A., Golish, D. R., Becker, K. J., Balram-Knutson, S. S., et al. (2019). The unexpected surface of asteroid (101955) Bennu. *Nature*, *568*(7750), 55–60. https://doi.org/10.1038/s41586-019-1033-6

Matsue, K., Yasui, M., Arakawa, M., & Hasegawa, S. (2020). Measurements of seismic waves induced by high-velocity impacts: Implications for seismic shaking surrounding impact craters on asteroids. *Icarus*, *338*, 113520. https://doi.org/10.1016/j.icarus.2019.113520

Michikami, T., Honda, C., Miyamoto, H., Hirabayashi, M., Hagermann, A., Irie, T., et al. (2019). Boulder size and shape distributions on asteroid Ryugu. *Icarus*, *331*, 179–191. https://doi.org/10.1016/j.icarus.2019.05.019

Moorhead, A. V. (2018). Deconvoluting measurement uncertainty from the meteor speed distribution. *Meteoritics & Planetary Science*, *53*(6), 1292–1298. https://doi.org/10.1111/maps.13066

Okawa, H., Arakawa, M., Yasui, M., Hasegawa, S., Toda, M., Shirai, K., & Yamamoto, Y. (2022). Effect of boulder size on ejecta velocity scaling law for cratering and its implication for formation of tiny asteroids. *Icarus*, 115212. https://doi.org/10.1016/j.icarus.2022

Sugita, S., Honda, R., Morota, T., Kameda, S., Sawada, H., Tatsumi, E., et al. (2019). The geomorphology, color, and thermal properties of Ryugu: Implications for parent-body processes. *Science*, *364*(6437), eaaw0422. https://doi.org/10.1126/science.aaw0422

Suzuki, A. I., Nakamura, A. M., Kadono, T., Wada, K., Yamamoto, S., & Arakawa, M. (2013). A formation mechanism for concentric ridges in eject surrounding impact craters in a layer of fine glass beads. *Icarus*, *225*(1), 298–307. https://doi.org/10.1016/j.icarus.2013.03.027

Tatsumi, E., & Sugita, S. (2018). Cratering efficiency on coarse-grain targets: Implications for the dynamical evolution of asteroid 25143 Itokawa. *Icarus*, *300*, 227–248. https://doi.org/10.1016/j.icarus.2017.09.004

Tsujido, S., Arakawa, M., Suzuki, A. I., & Yasui, M. (2015). Ejecta velocity distribution of impact craters formed on quartz sand: Effect of projectile density on crater scaling law. *Icarus*, *262*, 79–92. https://doi.org/10.1016/j.icarus.2015.08.035

Uehara, J. S., Ambroso, M. A., Ojha, R. P., & Durian, D. J. (2003). Low-speed impact craters in loose granular media. *Physical Review Letters*, *90*(19), 194301. https://doi.org/10.1103/PhysRevLett.90.194301

Watanabe, S., Hirabayashi, M., Hirata, N., Hirata, N. A., Noguchi, R., Shimaki, Y., et al. (2019). Hayabusa2 arrives at the carbonaceous asteroid 162173 Ryugu–A spinning top–shaped rubble pile. *Science*, *364*(6437), 268–272. https://doi.org/10.1126/science.aaz8032

Wünnemann, K., Nowka, D., Collins, G. S., Elbeshausen, D., & Bierhaus, M. (2010). Scaling impact crater formation on planetary surface – Insights from numerical simulation. In *Proceedings of 11th hypervelocity impact symposium 2010* (p. 120).

Yada, T., Abe, M., Okada, T., Nakato, A., Yogata, K., Miyazaki, A., et al. (2022). Preliminary analysis of the Hayabusa2 samples returned from C-type asteroid Ryugu. *Nature Astronomy*, *6*(2), 214–220. https://doi.org/10.1038/s41550-021-01550-6

Yasui, M., Arakawa, M., Okawa, H., & Hasegawa, S. (2022). Cratering experiments on granular targets with a variety of particle sizes: Implications for craters on rubble-pile asteroids. *Zenodo*. https://doi.org/10.5281/zenodo.6672869

Yasui, M., Arakawa, M., Yoshida, Y., Matsue, K., & Takano, S. (2020). Effects of oblique impacts on the impact strength of porous gypsum and glass spheres: Implications for the collisional disruption of planetesimals in thermal evolution. *Icarus*, *335*, 113414. https://doi.org/10.1016/j.icarus.2019.113414

Yasui, M., Matsumoto, E., & Arakawa, M. (2015). Experimental study on impact-induced seismic wave propagation through granular materials. *Icarus*, *260*, 320–331. https://doi.org/10.1016/j.icarus.2015.07.032